Hybrid Formulation of Wave Scattering in A Cracked Circular Cylinder

By

Abdel-Rahman Mahmoud

A Thesis

Submitted to the Faculty of Graduate Studies

in Partial Fulfillment of the Requirements

of the Degree of

MASTER OF SCIENCE

Department of Mechanical and Industrial Engineering

University of Manitoba

Winnipeg, Manitoba, Canada

National Library of Canada
Acquisitions and Bibliographic Services
395 Wellington Street
Ottawa ON K1A 0N4
Canada

Bibliothèque nationale du Canada
Acquisitions et services bibliographiques
395, rue Wellington
Ottawa ON K1A 0N4
Canada

Your file Votre référence

Our file Notre référence

0-612-76799-X

Canada

THE UNIVERSITY OF MANITOBA

FACULTY OF GRADUATE STUDIES

*****

COPYRIGHT PERMISSION PAGE

HYBRID FORMULATION OF WAVE SCATTERING IN A CRACKED CIRCULAR CYLINDER

BY

ABDEL-RAHMAN MAHMOUD

A Thesis/Practicum submitted to the Faculty of Graduate Studies of The University of Manitoba in partial fulfillment of the requirements of the degree

of

MASTER OF SCIENCE

To my parents, family and friends

Abstract

A hybrid method is used to analyze 3D wave scattering by inhomogeneities in an isotropic cylinder. The hybrid method is a technique that combines a finite element idealization of a bounded region containing the inhomogeneities and a wave function expansion outside. Continuity conditions for displacements and tractions are applied at discrete points on the common boundaries between the two regions. This results in a system of linear equations in the unknown wave function amplitudes. The solution gives the amplitudes which are used to obtain the reflection and transmission coefficients of the scattered wave fields. Satisfaction of reciprocity and the principle of energy conservation are used to check the validity and accuracy of the results. The model is calibrated against previously and independently obtained numerical as well as experimental data. Comparisons reveal excellent agreement between the current 3D hybrid model and a previous 2D hybrid model. On the other hand, the 3D hybrid model predicts somewhat lower values for the reflection and transmission coefficients compared with the quasi-exact method of Bai et al. A refined or non-uniform finite element mesh is likely to narrow this difference but at appreciable computational cost.

Acknowledgements

The author's gratitude and thanks are due to Professors A. H. Shah and N. Popplewell for their guidance, encouragement and support throughout the course of his study. The author deeply appreciates the fruitful discussions, invaluable suggestions and help of his colleague, Dr. H. Bai. The help and cooperation of the staff at the University of Manitoba High Performance Computing (HPC) Unit is highly appreciated. Financial support from the research grant of Prof. N. Popplewell and a teaching assistantship from the Mechanical and Industrial Engineering Department, University of Manitoba, enabled the author to complete his study. They are all acknowledged kindly.

Table of Contents

List of Figures

List of Tables

Chapter 1

Introduction

1.1 Nondestructive Evaluation of Cylinders

Cylinders are used widely in engineering applications. Cylindrical columns are used to support structures. Power transmission shafts in machines are nothing but cylinders. The conduits that carry fluids (gases or liquids) in power plants, refineries and nuclear reactors have mostly cylindrical shapes. In all these applications, cylindrical components are designed to sustain severe loading and environmental conditions. However, due to manufacturing defects or degradation during service, these components may fail. Their failure may be catastrophic. Hence, there is an imperative need to periodically inspect and monitor their structural integrity. The branch of science that deals with detecting flaws in structural and machine elements, without impairing their future serviceability, is known as *nondestructive evaluation* (NDE). There are several such techniques available in industry. They include:

1. ultrasonic testing,
2. eddy current and magnetic testing,
3. radiography,

4. visual (optical) testing,
5. microscopy,
6. nuclear magnetic resonance,
7. microwaves, and
8. thermography.

1.2 Ultrasonic Techniques

In ultrasonic NDE systems like the one shown in Figure 1.1, a transmitter launches (elastic) waves into a cylinder and a receiver measures the scattered signals from the internal flaw. A couplant placed between the specimen and the transmitter as well as the receiver ensures proper contact. The application of ultrasonic waves to detect flaws and inhomogeneities in a metal was suggested first in 1929 (Fredrick 1965). The fundamental concept upon which ultrasonic flaw detection is based is the *scattering* (reflection and transmission) of incident elastic waves by flaws and inhomogeneities. The advantages of ultrasonic nondestructive evaluation techniques include (McMaster 1959):

1. high sensitivity, permitting the detection of small defects;
2. great penetrating power that allows an examination of extremely thick sections;
3. accurate measurement of a flaw's position and size;
4. fast response that permits a rapid and automated inspection; and
5. easy access since only one surface of the specimen need be contacted.

Ultrasonic techniques may involve the use of *time-of-flight* measurement, *acoustic emission*, or *guided wave* techniques.

1.3 Guided Waves In Cylinders

There are several advantages of using guided waves in ultrasonic testing. First, the multimodal dispersive behavior of a guided wave can provide many data points in a given range of frequency (Rattanawangcharoen 1993). Second, the velocity of a guided wave is very sensitive to material properties.Third, the velocity of a guided wave is larger than the velocity of free waves (Rattanawangcharoen 1993) which makes it capable of reaching inaccessible areas (Rose and Quarry 1999). Certain (Lamb wave) modes do not suffer significant modification by a protective coating (Pan *et al.* 1999). This advantage can be used to inspect coated pipes without removing the coating layer.

The use of guided waves to detect cracks is an *inverse problem* in which a crack's location and geometry are to be determined from the scattered wave field. It is extremely difficult, if not impossible, to solve the inverse problem theoretically. However, a better understanding of the direct problem of scattering of elastic waves from simulated cracks would greatly help interpreting experimental ultrasonic test results.

A scattered wave field in a linearly elastic cylinder having a defect can be approximated by the modal summation of a finite number of normal modes that propagate in the undamaged cylinder. Hence, the study of elastic wave scattering must be preceded by a detailed study of the elastic wave propagation in cylinders.

1.4 Wave Propagation in Cylinders

The first analytical solution for elastic wave propagation in an infinite cylinder was obtained by Pochhammer (1876) and, independently, by Chree (1889). The Pochhammer-Chree solution satisfies the wave equation throughout a cylinder that has traction free boundary conditions on its lateral surfaces. Bancroft (1941) obtained the first numerical solutions for the Pochhammer-Chree dispersion equation for the case of compressional waves. Davies (1948) experimentally confirmed the Pochhammer-Chree

solution. Onoe et al (1962) computed numerical results over a wide range of frequencies for a finite set of real and complex wavenumbers for each individual frequency. Real wavenumbers correspond to the modes whose energies propagate in the cylinder. Complex wavenumbers, on the other hand, correspond to evanescent modes. It is worth mentioning that complex wavenumbers play an important role in the reflection and scattering of elastic waves from inhomogeneities. Several approximate methods have evolved to solve the Pochhammer-Chree dispersion equation because an exact solution is very difficult to obtain. Green (1964) summarized, in a review article, all the approximate methods available at that time. Gazis (1959) and Armenàkas et al (1969) presented a three dimensional (3D) solution of the Pochhammer-Chree equation based on elasticity formulations.

Many researchers (McNiven *et al.* 1963, Armenàkas 1967 and 1971, and Lai 1971) investigated, analytically, the dispersive characteristics of a number of perfectly bonded concentric isotropic cylinders using the theory of elasticity. The technique becomes impractical, however, for a large number of laminae. Rattanawangcharoen and Shah (1992a and 1992b) developed an efficient algorithm that circumvents this difficulty. In this algorithm, a propagator matrix imposes the displacement and stress continuity at the interfaces of the laminae based on a 3D elastic form of the dispersive relation. The numerical implementation used Muller's method (1956) with initial guesses obtained from a displacement based Rayleigh-Ritz approximation.

1.5 Scattering by a Crack in a Cylinder

Wave scattering occurs when an incident wave strikes a crack or an irregularity. The scattered field carries substantial information about the location, size and shape of the scatterers. This information may be inferred by comparing test results with theoretical predictions. However, few previous publications involve a theoretical study of elastic wave scattering by a crack in a cylinder because of the problem's geometric and computational complexity.

Oliver (1957) conducted the first study of wave scattering by cracks in cylinders. He investigated, experimentally, the free end reflection of axisymmetric waves in elastic rods. McNiven (1961) predicted the existence of an end resonant frequency using a 3-mode approximation. There is a difference of 13 percent between Oliver's experimental results and McNiven's approximations. McNiven and Shah (1967) investigated the influence of the end mode on the resonant frequencies of elastic hollow cylinders. They found that the hollow cylinder has lower end resonance frequency than the solid cylinder. Zemanek (1972) reconsidered McNiven's problem using 5-, 7-, and 9-mode approximations with a slightly higher Poisson's ratio. With a 9-mode approximation, Zemanek obtained an end resonant frequency that agreed very closely with Oliver's experimental findings. Several other techniques, such as an asymptotic expansion (Kim and Steele 1989), a least square method (Gregory and Gladwell 1989), and a hybrid model have been used successfully to solve this problem. The hybrid method will be reviewed in detail next.

1.6 The Hybrid Method

The hybrid method is a technique that combines a finite element idealization of a bounded region containing the crack and a wave function expansion in the exterior region. Continuity conditions of displacements and interactive forces are applied at discrete points on the common boundaries between the two regions. This procedure results in a system of linear equations in the unknown wave function amplitudes. These amplitudes are used to obtain the reflection and transmission coefficients of an incident wave.

A similar approach to the hybrid method was used in the 1970s by electrical engineers (McDonald and Wexler 1972, Mei 1974, and Chang and Mei 1976) to investigate the scattering of electromagnetic waves. Datta, Shah and Fortunko (1982) were able to apply the method to the field of elastic waves in their study of diffraction by edge cracks in a half-space. The first application to waveguides was made in 1982

(Abduljabbar *et al.*) in a study of the scattering of horizontally polarized shear (SH) waves by a symmetric crack in a plate.

Recently, the hybrid method has been used to study 2D wave scattering in a cylinder containing a finite axisymmetric region of inhomogeneity or a crack (Rattanawangcharoen *et al.* 1997). Zhuang *et al.* (1997) used a hybrid technique to investigate the scattering of elastic waves in a welded cylinder containing a circumferential crack. To the best of the author's knowledge, the application of the hybrid method to 3D elastic wave scattering in a cracked cylinder has not been reported yet.

1.7 Objectives

The main objective of the current study is to extend the hybrid method to the analysis of 3D wave scattering by a crack in a cylinder. The study is motivated by the need to solve, numerically, the problem of 3D scattering from *arbitrary geometric and material irregularities*. Since the hybrid technique applies the finite element idealization to the flawed region, it would be highly suitable for this purpose providing an appropriate meshing scheme is employed. However, the method is computationally demanding which hampers its implementation in three dimensions. Using a condensation scheme that confines the storage requirements only to the boundary nodal points is expected to partially circumvent this difficulty.

Numerical results will be presented for a linearly elastic isotropic cylinder with a weldment and/or symmetric, surface-breaking crack. The satisfaction of the reciprocity relations and the principle of energy conservation will be used to check the accuracy of the results. The validity will be finally confirmed by comparing results from the current study with previous, corresponding experimental findings and theoretical predictions.

1.8 Outline of Thesis

In this thesis, a hybrid formulation of 3D wave scattering in a cracked circular cylinder is investigated. Applications to practical problems are presented.

In Chapter 2, the propagation of elastic waves in an isotropic laminated cylinder is considered. The dispersion equation for the cylinder is derived. Then numerical solution techniques are presented and used in illustrative examples.

In Chapter 3, hybrid modeling of wave scattering by cracks in an elastic media is reviewed. A 3D formulation of the hybrid method is also presented. Procedures that are needed to validate and check the accuracy of the numerical procedure are outlined.

In Chapter 4, numerical results for wave scattering by symmetric surface breaking cracks in seamless as well as welded cylinders are presented. A comparison of these results with available theoretical predictions and experimental findings is performed.

Conclusions and recommendations for future work are given in *Chapter 5*.

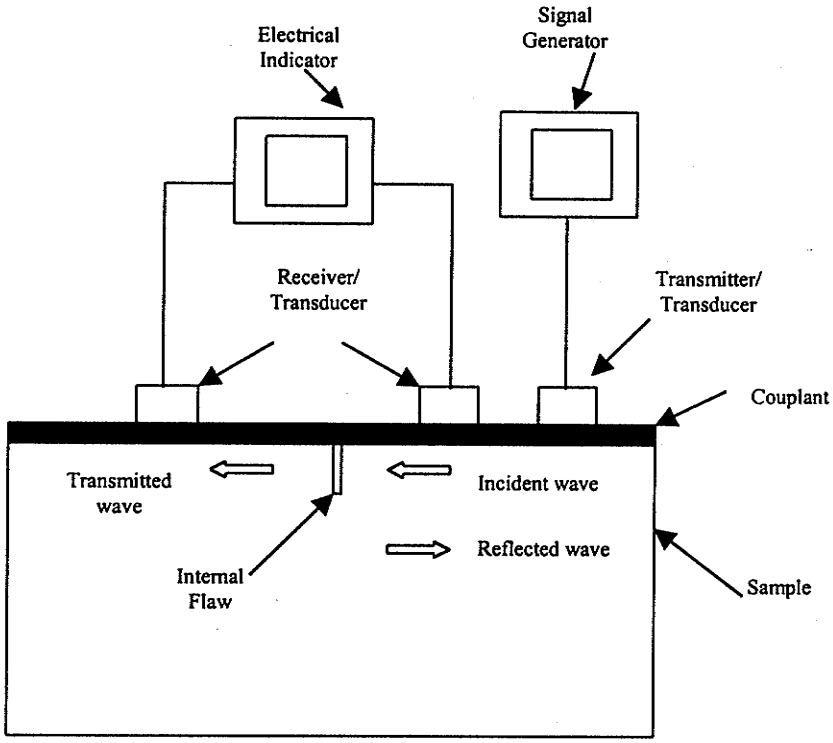

Figure 1.1. Schematic of ultrasonic test setup

Chapter 2

Elastic Wave Propagation in Isotropic Laminated Cylinders

Propagation of time harmonic elastic waves in an infinite, isotropic, laminated cylinder is considered in this chapter. The objective is to obtain dispersion characteristics of the cylinder, i.e. *the frequency and phase speed spectra.* The layers may have distinct mechanical properties as well as different thicknesses. The cylinder has the coordinate system shown in Figure 2.1. It has a mean radius R and a uniform thickness, H. The inner and the outer surfaces of the cylinder are assumed stress free. The complete cylinder is composed of cylindrical layers that are bonded perfectly. The inner and outer surfaces of each layer "l" are designated $\hat{r}_l$ and $\hat{r}_{l+1}$ respectively, as illustrated in Figure 2.1. Each layer is divided into a number of sublayers such that the total number of sublayers in the cylinder is N_s. The outer and inner surfaces of each sublayer "k" are designated r_k and r_{k+1}, respectively.

Two methodologies are used for elastic wave propagation in cylinders; a displacement based Rayleigh-Ritz approximation and an analytical method. The displacement based Rayleigh-Ritz approximation involves the formulation of the dispersion equation using Hamilton's principle. In the analytical method, which employs

the equations of linear elasticity, the exact dispersion relation is derived with the aid of propagator matrices. Roots of the approximate dispersion equation are found by solving a generalized eigenvalue problem. The eigenvalues correspond to the frequency ω, for a fixed wavenumber ξ or, alternately, the eigenvalue problem can be solved for ξ if ω is given. Approximate roots then serve as initial guesses in Muller's approach (Muller 1956) to solve the exact dispersion equation.

2.1 Description of the Problem

First, an approximate dispersion equation is formulated by using a displacement based, Rayleigh-Ritz approximation (Rattanawangcharoen *et. al.* 1992a and Bai 2001). This equation is used to calculate the frequency ω for a given wavenumber ξ, or alternatively for a given frequency ω to solve for the wavenumber ξ.

Second, an exact dispersion equation is formulated analytically using three-dimensional theory of elasticity (Rattanawangcharoen *et. al.* 1992a and Bai 2001). Roots of the exact dispersion equations are determined using Muller's method. Approximate roots, from the displacement based Rayleigh-Ritz approximation, are used as initial guesses in Muller's method.

2.2 Displacement Based, Rayleigh-Ritz Approximation

In a displacement based Rayleigh-Ritz approximation, the cylinder is divided into N_s sublayers. Displacement components u^r, u^θ and u^z are approximated over each sublayer by interpolation polynomials in the radial direction so that:

$$\boldsymbol{U}(r,\theta,z) = \boldsymbol{N}(\eta)\boldsymbol{Q}_e(\theta,z) \tag{2.1}$$

where,

$$\boldsymbol{U}^T = \left\langle u^r \quad u^\theta \quad u^z \right\rangle, \tag{2.2}$$

$$\boldsymbol{Q}_e^T = \left\langle \boldsymbol{U}_b^T \quad \boldsymbol{U}_m^T \quad \boldsymbol{U}_f^T \right\rangle, \tag{2.3}$$

in which a *"T"* superscript denotes the transpose, and

$$\boldsymbol{N} = \begin{bmatrix} n_1 & 0 & 0 & n_2 & 0 & 0 & n_3 & 0 & 0 \\ 0 & n_1 & 0 & 0 & n_2 & 0 & 0 & n_3 & 0 \\ 0 & 0 & n_1 & 0 & 0 & n_2 & 0 & 0 & n_3 \end{bmatrix}. \tag{2.4}$$

In equation (2.1) through (2.3), the nodal displacements $\boldsymbol{U}_b, \boldsymbol{U}_m$ and $\boldsymbol{U}_f$ are taken at the back (inner), middle and front (outer) nodal surfaces of a sublayer. The interpolation polynomials, n_i, are quadratic functions given by:

$$n_1 = \frac{1}{2}\left(\eta^2 - \eta\right); \quad n_2 = 1 - \eta^2; \quad n_3 = \frac{1}{2}\left(\eta^2 + \eta\right) \tag{2.5a}$$

where

$$\eta = \frac{2r - r_k - r_{k+1}}{h_k} \tag{2.5b}$$

and h_k is the thickness of the k^{th} sublayer.

By using Hamilton's principle, the Lagrangian, $\boldsymbol{L}_k$, for the k^{th} sublayer is calculated as:

$$\boldsymbol{L}_k = \frac{1}{2} \int_t \int_z \int_\theta \left\{ \int_{r_k}^{r_{k+1}} \left[\rho\omega^2 \bar{\boldsymbol{U}}^T \boldsymbol{U} - \bar{\boldsymbol{\varepsilon}}^T \boldsymbol{C} \boldsymbol{\varepsilon} \right] r dr \right\} d\theta dz dt \tag{2.6}$$

where an overbar indicates a complex conjugate; a dot denotes differentiation with respect to time t; ρ is the material density of sublayer k and $\boldsymbol{C}$ is its elasticity matrix. The latter is defined as:

$$\boldsymbol{C}=\begin{bmatrix} \lambda+2\mu & \lambda & \lambda & 0 & 0 & 0 \\ \lambda & \lambda+2\mu & \lambda & 0 & 0 & 0 \\ \lambda & \lambda & \lambda+2\mu & 0 & 0 & 0 \\ 0 & 0 & 0 & \mu & 0 & 0 \\ 0 & 0 & 0 & 0 & \mu & 0 \\ 0 & 0 & 0 & 0 & 0 & \mu \end{bmatrix} \tag{2.7}$$

in which λ and μ are Lamé's constants. Moreover ε is the strain vector defined, in terms of the displacement, by (Bai 2001):

$$\varepsilon=\boldsymbol{P}_r\frac{\partial \boldsymbol{U}}{\partial r}+\frac{1}{r}\boldsymbol{P}_\theta\frac{\partial \boldsymbol{U}}{\partial \theta}+\boldsymbol{P}_z\frac{\partial \boldsymbol{U}}{\partial z}+\frac{1}{r}\boldsymbol{P}_0\boldsymbol{U} \tag{2.8a}$$

where

$$\varepsilon=\left\langle \varepsilon^{rr} \quad \varepsilon^{\theta\theta} \quad \varepsilon^{zz} \quad \gamma^{\theta z} \quad \gamma^{zr} \quad \gamma^{r\theta} \right\rangle^T \tag{2.8b}$$

and

$$\boldsymbol{P}_r=[\boldsymbol{e}_1,\boldsymbol{e}_6,\boldsymbol{e}_5],\ \boldsymbol{P}_\theta=[\boldsymbol{e}_6,\boldsymbol{e}_2,\boldsymbol{e}_4],\ \boldsymbol{P}_z=[\boldsymbol{e}_5,\boldsymbol{e}_4,\boldsymbol{e}_3],\ \boldsymbol{P}_0=[\boldsymbol{e}_2,-\boldsymbol{e}_6,0]. \tag{2.8c}$$

The $\boldsymbol{e}_i\,(i=1..6)$ are the fundamental unit column vectors in $\boldsymbol{R}^6$; $\boldsymbol{P}_r,\boldsymbol{P}_\theta,\boldsymbol{P}_z$ and $\boldsymbol{P}_0$ are six by three real matrices and a "T"superscript represents the transpose. Substituting equation (2.1) into equation (2.8a) gives the strain vector as,

$$\varepsilon=\boldsymbol{B}_r\boldsymbol{U}+\boldsymbol{B}_\theta\frac{\partial \boldsymbol{U}}{\partial \theta}+\boldsymbol{B}_z\frac{\partial \boldsymbol{U}}{\partial z} \tag{2.9a}$$

where

$$\boldsymbol{B}_r = \boldsymbol{P}_r \frac{d\boldsymbol{N}}{dr} + \boldsymbol{P}_0, \quad \boldsymbol{B}_\theta = \frac{1}{r}\boldsymbol{P}_\theta \boldsymbol{N}, \quad \boldsymbol{B}_z = \frac{1}{r}\boldsymbol{P}_z \boldsymbol{N}. \tag{2.9b}$$

By substituting equations (2.1) and (2.9a) in equation (2.6), the Lagrangian can be written in terms of the generalized nodal displacements given in equation (2.3). For a time harmonic wave of the form $e^{-j\omega t}$, where ω is the circular frequency, upon setting the first variation of the summation of the contributions from all sublayers to zero, the governing equation for the entire cylinder is obtained as (Bai 2001):

$$\boldsymbol{K}_{rr}\boldsymbol{Q} + \boldsymbol{K}_\theta \boldsymbol{Q}_{,\theta} + \boldsymbol{K}_z \boldsymbol{Q}_{,z} - \boldsymbol{K}_{\theta\theta}\boldsymbol{Q}_{,\theta\theta} - \boldsymbol{K}_{z\theta}\boldsymbol{Q}_{,z\theta} - \boldsymbol{K}_{zz}\boldsymbol{Q}_{,zz} - \omega^2 \boldsymbol{M}\boldsymbol{Q} = 0. \tag{2.10}$$

where a comma subscript denotes partial derivative(s) with respect to the adjacent variable(s). The matrices $\boldsymbol{K}_{rr}$, $\boldsymbol{K}_{\theta\theta}, \boldsymbol{K}_{z\theta}, \boldsymbol{K}_{zz}$ and $\boldsymbol{M}$ are real and symmetric, $\boldsymbol{K}_\theta$ and $\boldsymbol{K}_z$ are anti-symmetric. They are given by:

$$\boldsymbol{M} = 2\pi \int_{R_i}^{R_o} \rho \boldsymbol{N}^T \boldsymbol{N}\, r dr \tag{2.11}$$

$$\boldsymbol{K}_{ii} = 2\pi \int_{R_i}^{R_o} \boldsymbol{B}_i^T \boldsymbol{C} \boldsymbol{B}_i\, r dr, \quad i = r, \theta, z \tag{2.12}$$

$$\boldsymbol{K}_{\theta z} = 2\pi \int_{R_i}^{R_o} \left(\boldsymbol{B}_\theta^T \boldsymbol{C} \boldsymbol{B}_z + \boldsymbol{B}_z^T \boldsymbol{C} \boldsymbol{B}_\theta \right) r dr \tag{2.13}$$

and

$$\boldsymbol{K}_j = 2\pi \int_{R_i}^{R_o} \left(\boldsymbol{B}_r^T \boldsymbol{C} \boldsymbol{B}_j - \boldsymbol{B}_j^T \boldsymbol{C} \boldsymbol{B}_r \right) r dr \qquad j = \theta, z \tag{2.14}$$

where $\boldsymbol{C}$ is the elasticity matrix, given by equation (2.7), the $\boldsymbol{B}_i\left(i=r,\theta,z\right)$ are given by equation (2.9b), and $\boldsymbol{Q}$ contains the nodal displacements along one radius of the cylinder.

For a wave propagating in the positive $z-$direction, the solution of equation (2.10) can be assumed to take the form:

$$\boldsymbol{Q}=\boldsymbol{Q}_o e^{j(m\theta+\xi z)} \tag{2.15}$$

where $j=\sqrt{-1}$ and $\boldsymbol{Q}_0$ represents the nodal amplitude vector. Substituting equation (2.15) into equation (2.10) results in the following set of linear homogeneous algebraic equations:

$$\begin{bmatrix} 0 & \boldsymbol{I} \\ \omega^2\boldsymbol{M}-\boldsymbol{K}_2 & j\boldsymbol{K}_1 \end{bmatrix}\begin{Bmatrix} \boldsymbol{Q}_0 \\ \xi\boldsymbol{Q}_0 \end{Bmatrix}=\xi\begin{bmatrix} \boldsymbol{I} & \boldsymbol{0} \\ \boldsymbol{0} & \boldsymbol{K}_0 \end{bmatrix}\begin{Bmatrix} \boldsymbol{Q}_0 \\ \xi\boldsymbol{Q}_0 \end{Bmatrix} \tag{2.16}$$

where $\boldsymbol{I}$ is the identity matrix, and

$$\boldsymbol{K}_0=\boldsymbol{K}_{zz},\ \boldsymbol{K}_1=jm\boldsymbol{K}_{z\theta}-\boldsymbol{K}_z,\ \boldsymbol{K}_2=m^2\boldsymbol{K}_{\theta\theta}+jm\boldsymbol{K}_\theta+\boldsymbol{K}_{rr}. \tag{2.17}$$

This results in a quadratic algebraic eigenvalue problem which serves as the approximate dispersion relation for the cylinder.

2.3 Analytical Method

2.3.1 Hollow Cylinder

Using the Helmholtz resolution (Morse and Feshback 1953), the displacement field in cylindrical coordinates can be written in terms of the Lamé potential functions, Φ and $\boldsymbol{H}$, as:

$$\boldsymbol{U} = \nabla\Phi + \nabla\times\boldsymbol{H} \qquad \nabla.\boldsymbol{H} = F(\boldsymbol{x},t) \tag{2.18}$$

where $F(\boldsymbol{x},t)$ is an arbitrary function arising from the gauge invariance of the resolution (Morse and Feshback 1953 and Gazis 1959). If cylindrical coordinates are used so that $\boldsymbol{H} \equiv (H_r, H_\theta, H_z)$ the corresponding components of the displacement field, $\boldsymbol{U} \equiv (u^r, u^\theta, u^z)$, are given by:

$$u^r = \frac{\partial\Phi}{\partial r} + \frac{1}{r}\frac{\partial H_z}{\partial\theta} - \frac{\partial H_\theta}{\partial z} \tag{2.19a}$$

$$u^\theta = \frac{1}{r}\frac{\partial\Phi}{\partial\theta} + \frac{\partial H_r}{\partial z} - \frac{\partial H_z}{\partial r} \tag{2.19b}$$

$$u^z = \frac{\partial\Phi}{\partial z} + \frac{1}{r}\frac{\partial}{\partial r}(rH_\theta) - \frac{1}{r}\frac{\partial H_r}{\partial\theta}. \tag{2.19c}$$

Consequently, the scalar potential Φ and vector potential $\boldsymbol{H}$ satisfy the following scalar and vector wave equations:

$$\nabla^2\Phi = \frac{1}{c_p^{\,2}}\frac{\partial^2\Phi}{\partial t^2} \tag{2.20a}$$

and

$$\nabla^2 \boldsymbol{H} = \frac{1}{c_s^{\,2}} \frac{\partial^2 \boldsymbol{H}}{\partial t^2} \tag{2.20b}$$

where ∇^2 is the Laplacian operator. The c_p and c_s are the speeds of the dilatational and distortional waves, respectively. They are defined as:

$$c_p^2 = \frac{\lambda + 2\mu}{\rho} \qquad \text{and} \qquad c_s^2 = \frac{\mu}{\rho}. \tag{2.21}$$

The expanded forms of the left hand side of equations (2.20a) and (2.20b) are:

$$\nabla^2 \Phi = \frac{\partial^2 \Phi}{\partial r^2} + \frac{1}{r}\frac{\partial \Phi}{\partial r} + \frac{1}{r^2}\frac{\partial^2 \Phi}{\partial \theta^2} + \frac{\partial^2 \Phi}{\partial z^2} \tag{2.22a}$$

and

$$\nabla^2 \boldsymbol{H} = \left(\nabla^2 H_r - \frac{H_r}{r^2} - \frac{2}{r^2}\frac{\partial H_\theta}{\partial \theta}\right)\boldsymbol{e}_r + \left(\nabla^2 H_\theta - \frac{H_\theta}{r^2} + \frac{2}{r^2}\frac{\partial H_r}{\partial \theta}\right)\boldsymbol{e}_\theta + \nabla^2 H_z \boldsymbol{e}_z \tag{2.22b}$$

where $\boldsymbol{e}_r$, $\boldsymbol{e}_\theta$, and $\boldsymbol{e}_z$ are unit vectors in the r, θ, and z directions, respectively. Any solution must satisfy the boundary conditions that the outer and inner surfaces of the cylinder are free of stress. Mathematically this requirement can be written as

$$\sigma^{rr} = \sigma^{r\theta} = \sigma^{rz} = 0 \qquad \text{at} \qquad r = R_i, R_o. \tag{2.23}$$

Assume that a harmonic wave is propagating in the positive z-direction. Then Φ and $\boldsymbol{H}$ take the form:

$$\Phi = f_\Phi(r) e^{jm\theta} e^{j(\xi z - \omega t)} \tag{2.24a}$$

$$H_r = f_r(r) e^{jm\theta} e^{j(\xi z - \omega t)} \tag{2.24b}$$

$$H_\theta = f_\theta(r) e^{jm\theta} e^{j(\xi z - \omega t)} \tag{2.24c}$$

$$H_z = f_z(r)e^{jm\theta}e^{j(\xi z-\omega t)}. \tag{2.24d}$$

where the $f_i(r)$, $i=\Phi,r,\theta,z$, have to be determined still. The equations of motion (2.20) are satisfied if:

$$f_\Phi'' + \frac{1}{r}f_\Phi' + \left(\alpha^2 - \frac{m^2}{r^2}\right)f_\Phi = 0 \tag{2.25a}$$

$$f_r'' + \frac{1}{r}f_r' + \left(\beta^2 - \frac{(m+1)^2}{r^2}\right)f_r = 0 \tag{2.25b}$$

$$f_z'' + \frac{1}{r}f_z' + \left(\beta^2 - \frac{m^2}{r^2}\right)f_z = 0 \tag{2.25c}$$

where a prime superscript denotes differentiation with respect to r while

$$\alpha^2 = \frac{\omega^2}{c_p^2} - \xi^2 \qquad \text{and} \qquad \beta^2 = \frac{\omega^2}{c_s^2} - \xi^2 \tag{2.26}$$

and $f_\theta(r) = -jf_r(r)$. The solution of equation (2.24) can be obtained in terms of Hankel functions (Rattanawangcharoen *et al.* 1992a) as:

$$f_\Phi(r) = A_1H_m^{(1)}(\alpha r) + B_1H_m^{(2)}(\alpha r), \tag{2.27a}$$

$$f_r(r) = A_2H_{m+1}^{(1)}(\beta r) + B_2H_{m+1}^{(2)}(\beta r), \tag{2.27b}$$

$$f_z(r) = A_3H_m^{(2)}(\beta r) + B_3H_m^{(2)}(\beta r) \tag{2.27c}$$

in which A_1, A_2, A_3, B_1, B_2, and B_3 are arbitrary complex constants for the sublayer; $H_m^{(1)}$ and $H_m^{(2)}$ are, respectively, the *mth* order Hankel functions of the first and second kind; and $H_{m+1}^{(1)}$ and $H_{m+1}^{(2)}$ are the corresponding $(m+1)th$ order Hankel functions.

The generalized Hooke's law gives the stress components as:

$$\sigma^{ij} = \lambda\Delta\delta_{ij} + 2\mu\varepsilon^{ij} \qquad i, j = r, \theta, z \tag{2.28}$$

where δ_{ij} and Δ are defined by:

$$\delta_{ij} \equiv \text{Kronecker delta} = \begin{cases} 1 & i = j \\ 0 & i \neq j \end{cases}$$

and

$$\Delta = \frac{\partial u^r}{\partial r} + \frac{u^r}{r} + \frac{1}{r}\frac{\partial u^\theta}{\partial \theta} + \frac{\partial u^z}{\partial z}.$$

By substituting equation (2.27) into equations (2.24) and (2.19) and, in turn, into equations (2.8a) and (2.28), the displacement and stress components at the interface $r = r_k$ can be represented as:

$$\begin{Bmatrix} \boldsymbol{U}_k \\ \boldsymbol{S}_k \end{Bmatrix} = \boldsymbol{Q}_k \begin{Bmatrix} \boldsymbol{A} \\ \boldsymbol{B} \end{Bmatrix} \tag{2.29}$$

where

$$\boldsymbol{U}_k^T = \langle u_k^r \quad u_k^\theta \quad u_k^z \rangle, \quad \boldsymbol{S}_k^T = \langle \sigma_k^{rr} \quad \sigma_k^{r\theta} \quad \sigma_k^{rz} \rangle \tag{2.30a}$$

$$\boldsymbol{A}^T = \langle A_1 \quad A_2 \quad A_3 \rangle, \quad \boldsymbol{B}^T = \langle B_1 \quad B_2 \quad B_3 \rangle. \tag{2.30b}$$

The six by six matrix, $\boldsymbol{Q}_k$, contains the Hankel functions $H_m^{(1)}$ and $H_m^{(2)}$. It is detailed in *Appendix A*.

Similarly, the evaluation of the displacements and stresses at the interface, $r = r_{k+1}$, of the k^{th} layer yields:

$$\begin{Bmatrix} U_{k+1} \\ S_{k+1} \end{Bmatrix} = Q_{k+1} \begin{Bmatrix} A \\ B \end{Bmatrix}. \tag{2.31}$$

By eliminating the arbitrary coefficients from equations (2.29) and (2.31), the following relations can be obtained between the displacements and stresses at the interfaces of the k^{th} sublayer:

$$\begin{Bmatrix} U_{k+1} \\ S_{k+1} \end{Bmatrix} = P_k \begin{Bmatrix} U_k \\ S_k \end{Bmatrix} \tag{2.32}$$

where

$$P_k = Q_{k+1} Q_k^{-1}. \tag{2.33}$$

The six by six matrix P_k is the *propagator matrix* for the k^{th} sublayer. Repeated application of equation (2.33) to each successive sublayer of the cylinder's N_s sublayers gives:

$$\begin{Bmatrix} U_{N_s+1} \\ S_{N_s+1} \end{Bmatrix} = P \begin{Bmatrix} U_1 \\ S_1 \end{Bmatrix} \tag{2.34}$$

where

$$P = P_{N_s} \quad P_{N_s-1} \quad . \quad . \quad . \quad P_1. \tag{2.35}$$

The matrix P can be divided into four three-by-three sub-matrices as follows:

$$P = \begin{bmatrix} P_{11} & P_{12} \\ P_{21} & P_{22} \end{bmatrix}. \tag{2.36}$$

Invoking in equation (2.34) the zero traction boundary conditions at the innermost and outermost surfaces of the cylinder $\left(\text{i.e. } \boldsymbol{S}_{N_s+1} = \boldsymbol{S}_1 = \{0\}\right)$ leads to:

$$\boldsymbol{P}_{21}\boldsymbol{U}_1 = \{0\}. \tag{2.37}$$

Then the exact dispersion relation can be obtained by equating the determinant of the coefficient matrix to zero, i.e.:

$$|\boldsymbol{P}_{21}| = 0. \tag{2.38}$$

2.3.2 Solid Cylinder

For the special case of a solid circular cylinder, Bessel functions of the second kind, Y_m, tend to infinity as r approaches zero. Hence, the solution (which corresponds to equation (2.27)) becomes:

$$f_\Phi(r) = C_1 J_m(\alpha r), \tag{2.39a}$$

$$f(r)_r = C_2 J_{m+1}(\beta r), \tag{2.39b}$$

$$f_z(r) = C_3 J_m(\beta r) \tag{2.39c}$$

for the innermost (i.e. first) sublayer of the solid rod which is bounded by $r = 0$ and $r = r_1$. Moreover, J_m is the Bessel function of the first kind. The C_1, C_2 and C_3 are arbitrary constants for the innermost sublayer. The displacement and stress components at the interface $r = r_1$, $\boldsymbol{U}_1$ and $\boldsymbol{S}_1$ respectively, can be written in terms of these constants as:

$$\boldsymbol{U}_1 = \boldsymbol{R}\boldsymbol{C} \tag{2.40a}$$

$$\boldsymbol{S}_1 = \boldsymbol{T}\boldsymbol{C} \tag{2.40b}$$

where

$$\boldsymbol{C} = \langle C_1 \quad C_2 \quad C_3 \rangle . \tag{2.40c}$$

The $\boldsymbol{R}$ and $\boldsymbol{T}$ are three by three matrices that contain the Bessel function J_m. They are given in *Appendix A*. The stiffness matrix $\boldsymbol{K}$, which relates the stresses to the displacements, can be determined by combining equations (2.40a) and (2.40b) to eliminate $\boldsymbol{C}$. Then

$$\boldsymbol{S}_l = \boldsymbol{T}\boldsymbol{R}^{-1}\boldsymbol{U}_l = \boldsymbol{K}\boldsymbol{U}_l \tag{2.40d}$$

where $\boldsymbol{K} = \boldsymbol{T}\boldsymbol{R}^{-1}$ Applying the propagator matrix between the first and last interfaces gives:

$$\begin{Bmatrix} \boldsymbol{U}_{N_s+1} \\ \boldsymbol{S}_{N_s+1} \end{Bmatrix} = \begin{bmatrix} \boldsymbol{P}_{11} + \boldsymbol{P}_{12}\boldsymbol{K} \\ \boldsymbol{P}_{21} + \boldsymbol{P}_{22}\boldsymbol{K} \end{bmatrix} \boldsymbol{U}_1 . \tag{2.41}$$

By invoking the traction free boundary conditions at the outer radius of the solid cylinder, the analogous dispersion relation to equation (2.38) can be written as:

$$\left| \boldsymbol{P}_{21} + \boldsymbol{P}_{22}\boldsymbol{K} \right| = 0 . \tag{2.42}$$

2.4 Roots of Dispersion Equation

For a fixed value of frequency ω or wavenumber ξ, the exact dispersion relations (2.38) and (2.42) are transcendental functions of either ξ or ω, respectively. It is possible to evaluate the roots of these equations by using a "brute force" search method. This approach is computationally demanding as the roots are complex and sparse. Instead,

Muller's method is used as it requires less computational time when initial guesses from a displacement based Rayleigh-Ritz approximation are employed.

2.5 Spectra of Frequency and Phase Speed

Numerical results are presented next for two illustrative examples. The first example is a steel pipe that was investigated both experimentally and numerically by Alleyne *et al.* (1998) and Lowe *et al.* (1998), respectively. The second example is a steel pipe that has been studied numerically by Zhuang *et al.* (1997).

Example 2.1

The cylinder's material in this example has a modulus of elasticity, E, and Poisson ratio, ν, of 216.9 GPa and 0.287, respectively. The longitudinal and torsional wave speeds are $c_p = 32.6\times10^3\ m/s$ and $c_s = 5.96\times10^3\ m/s$. The inner radius, R_i, and the thickness, H, of the cylinder are 38 mm and 5.5 mm respectively. Therefore, the thickness-to-mean radius ratio, H/R, is 0.135. The geometrical data and material properties are summarized in Table 2.1. Frequency spectra for a longitudinal wave ($m=0$) and a flexural wave ($m=1$) are shown in Figure 2.2. In this figure the non-dimensional wavenumber and frequency are defined as:

$$\Omega = \frac{\omega}{\omega_{ref}} \quad \text{and} \quad \gamma = \frac{\xi}{\xi_{ref}} \tag{2.43}$$

where,

$$\omega_{ref} = \frac{1}{H}\sqrt{\frac{\mu}{\rho}} \quad \text{and} \quad \xi_{ref} = \frac{1}{H}. \tag{2.44}$$

Dispersion curves are shown in Figure 2.3 over a frequency range from 0 to 750 kHz. The asymptotic behavior of the phase speed curves is apparent at high frequencies. For example, modes $L(0,1), L(0,2), F(1,1), F(1,2), F(1,3)$ and $F(1,4)$ have a common

asymptotic phase speed of approximately 4 $\mu m/s$. The distinctive feature of the longitudinal and flexural modes coinciding over a wide range of frequencies is pronounced in two cases: (a) $L(0,1)$ and $F(1,1)$ as well as (b) $L(0,2)$ and $F(1,3)$. For modes other than $L(0,1)$, the phase speed curves increase sharply at their cutoff frequencies. The explanation is that when the wavenumber approaches zero (i.e. the wavelength approaches infinity), the phase speed approaches infinity at the cutoff frequency. The nondispersive behavior of modes $L(0,2), F(1,2)$ and $F(1,3)$ is evident in the frequency ranges 25-125 *kHz*, 25-350 *kHz* and 75-125 *kHz* respectively. It is desirable since the travel distance then does not affect the wave speed as the wave propagates in the cylinder. (Note that the attenuation capacity of a cylinder's material itself is neglected here.)

Example 2.2

The cylinder's material in this example has a modulus of elasticity, E, and Poisson ratio, ν, of 211.7 *GPa* and 0.29 respectively. The longitudinal and torsional wave speeds are $c_p = 35.6\times10^3\ m/s$ and $c_s = 5.88\times10^3\ m/s$. The inner radius, R_i, and the thickness, H, of the cylinder are 48.26 *mm* and 5.08 *mm* respectively. Therefore, the thickness-to-mean radius ratio, H/R, is 0.1. The geometrical data and material properties are summarized in Table 2.2. Frequency spectra for $m = 0$ and 1 are shown in Figure 2.4. Dispersion curves are presented in Figure 2.5 over a frequency range from 0 to 750 kHz. The frequency spectra and dispersion curves are similar to the previous example.

The wave modes in the undamaged cylinder determined in this chapter will be used in the modal summation representation of the scattered wave fields in the following chapter.

Table 2.1. Geometric and material properties for Example 2.1

PROPERTY	VALUE
H, mm	5.50
H/R	0.135
μ, Gpa	84.29
λ, Gpa	113.15
ρ, kg/m^3	793.19

Table 2.2. Geometric and material properties for Example 2.2

PROPERTY	VALUE
H, mm	5.08
H/R	0.100
μ, Gpa	82.00
λ, Gpa	112.00
ρ, kg/m^3	780.00

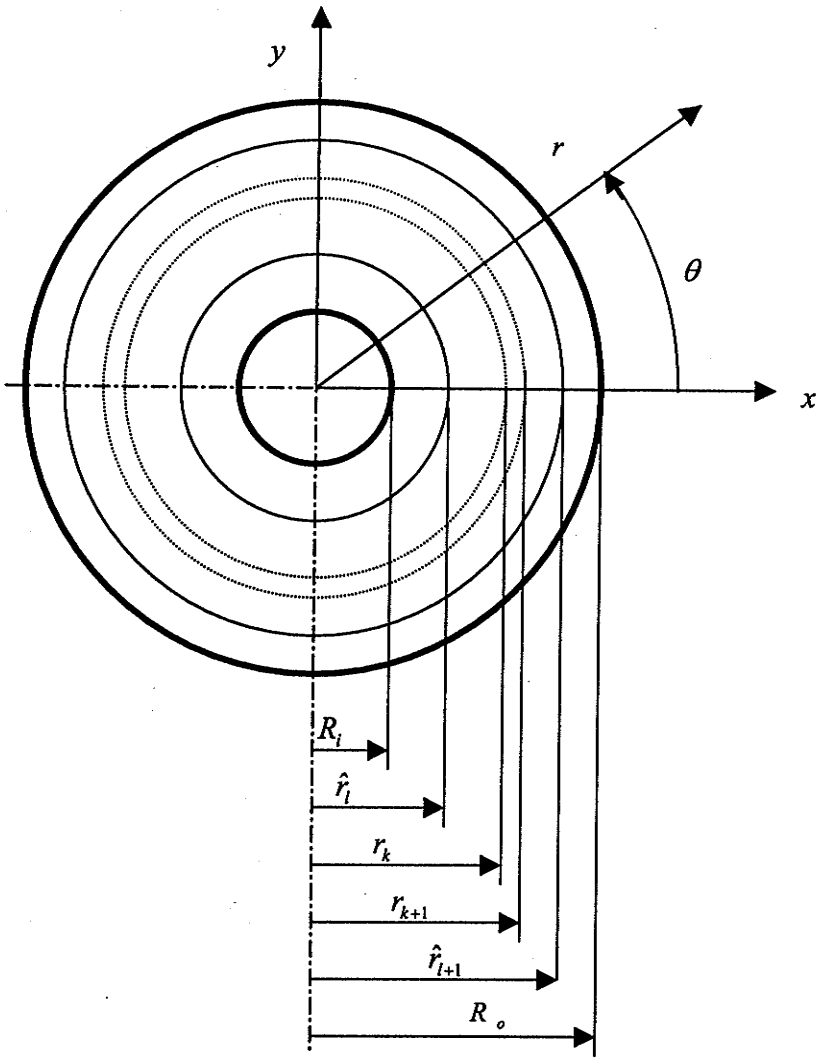

Figure 2.1. Cross section of a laminated cylinder

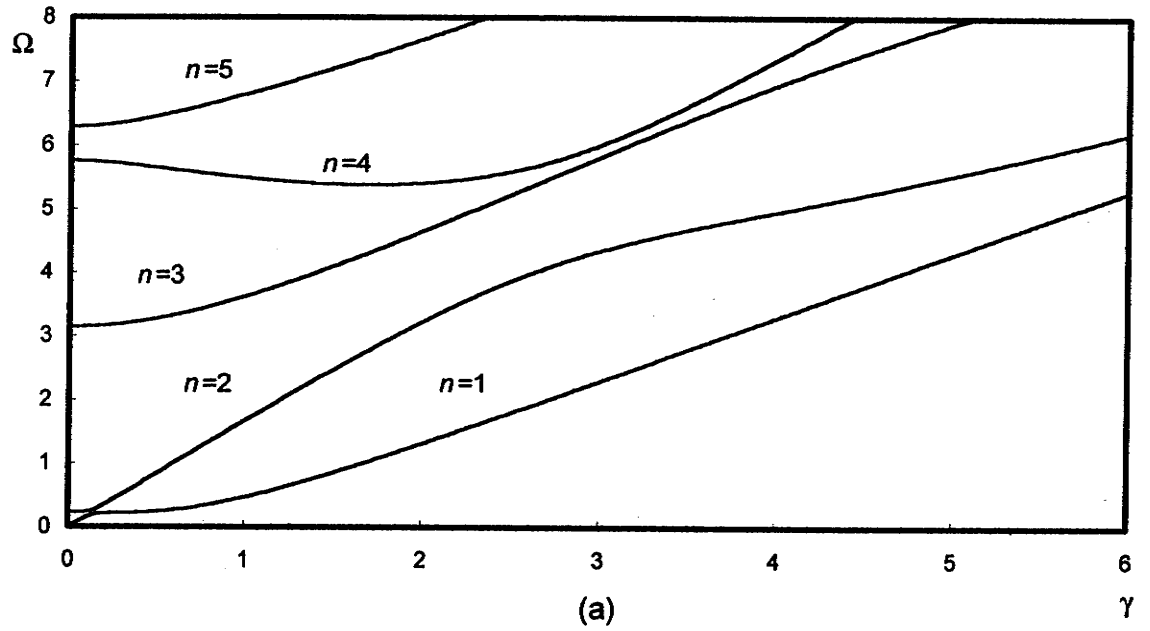

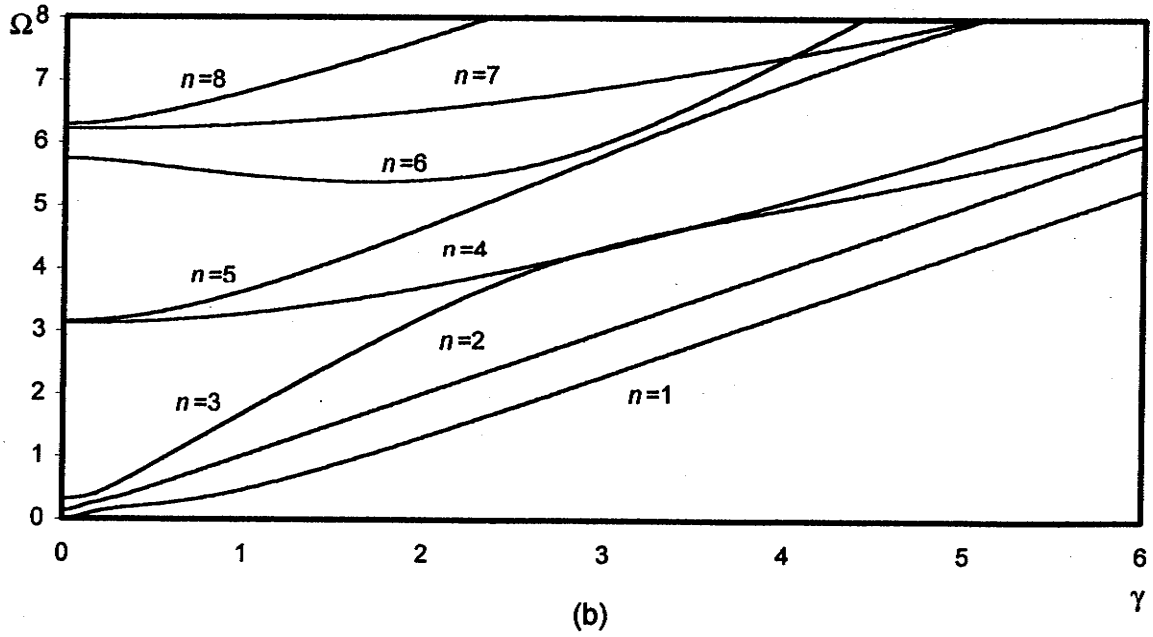

Figure 2.2. Frequency spectrum of a steel pipe. H/R = 0.135 and ν =0.287. (a) Longitudinal wave (m=0), and (b) flexural wave (m=1)

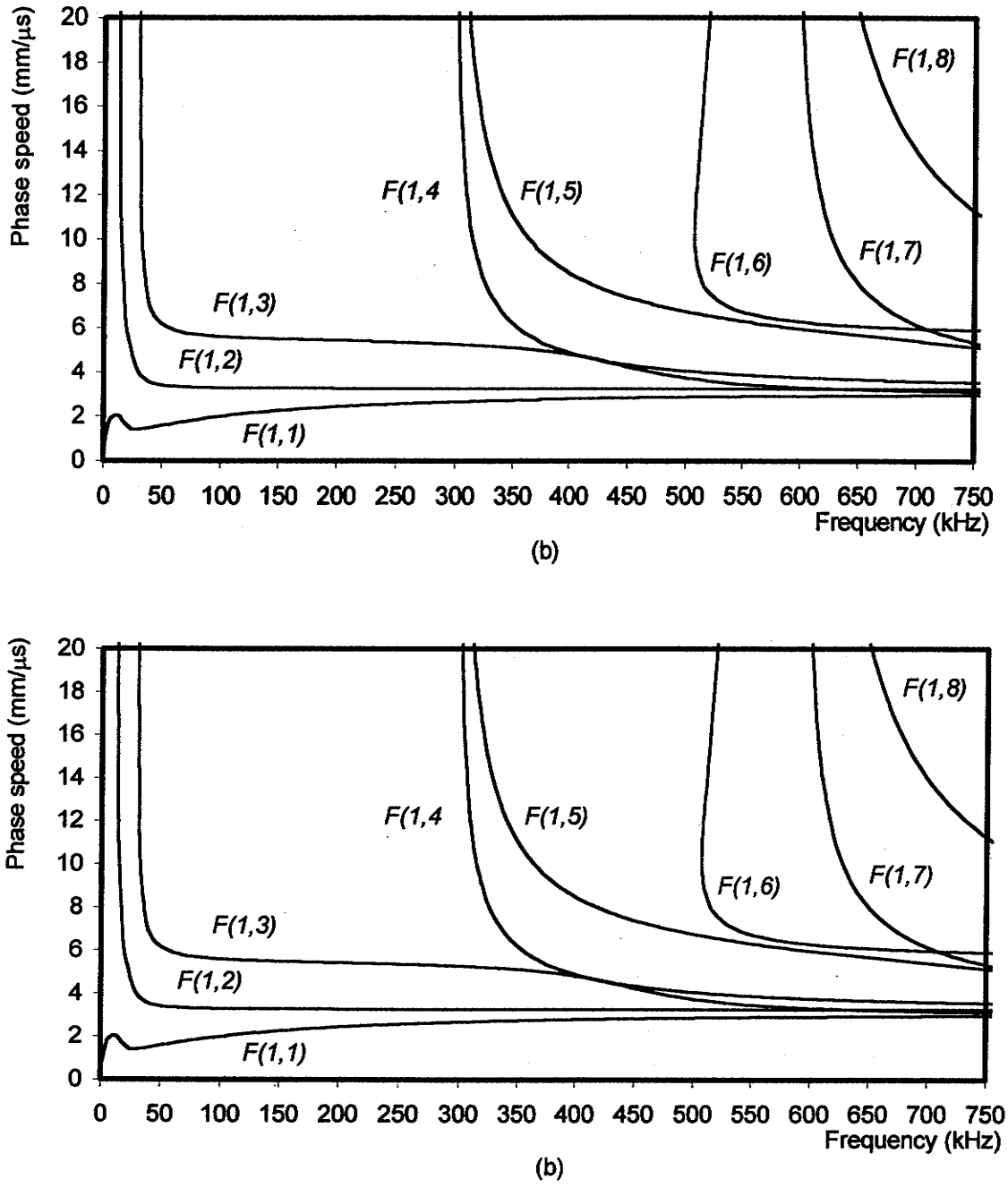

Figure 2.3. Phase speed as a function of frequency for a steel pipe. $H/R = 0.135$ and $\nu = 0.287$. (a) Longitudinal wave (m=0), and (b) flexural wave (m=1)

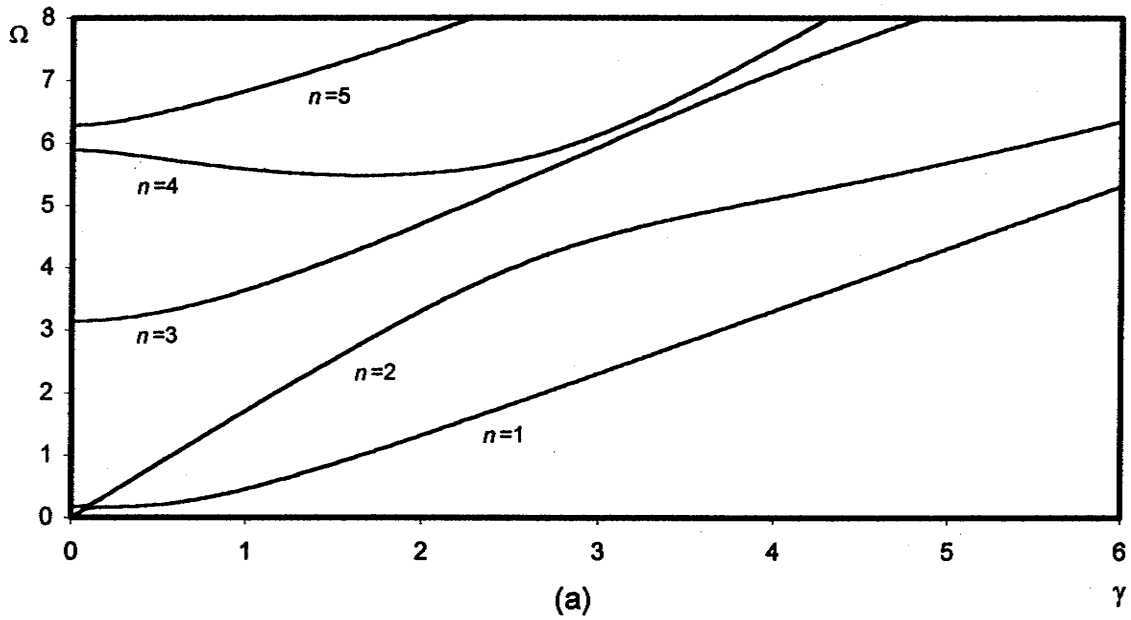

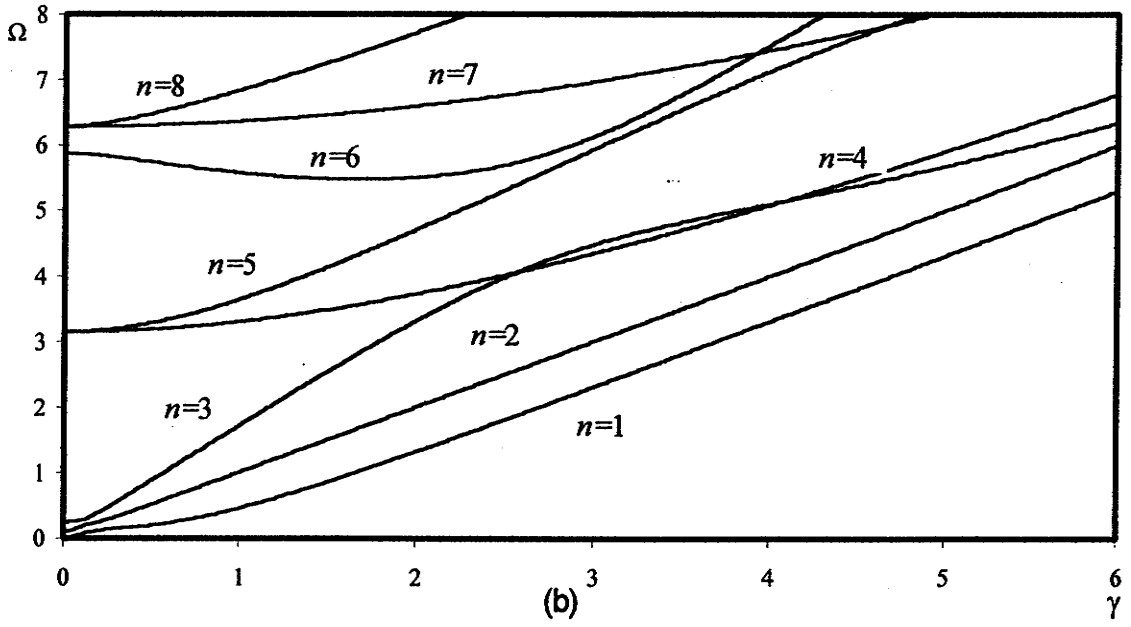

Figure 2.4. Frequency spectrum of a steel pipe. H/R = 0.1 and ν =0.29. (a) Longitudinal wave (m=0), and (b) flexural wave (m=1)

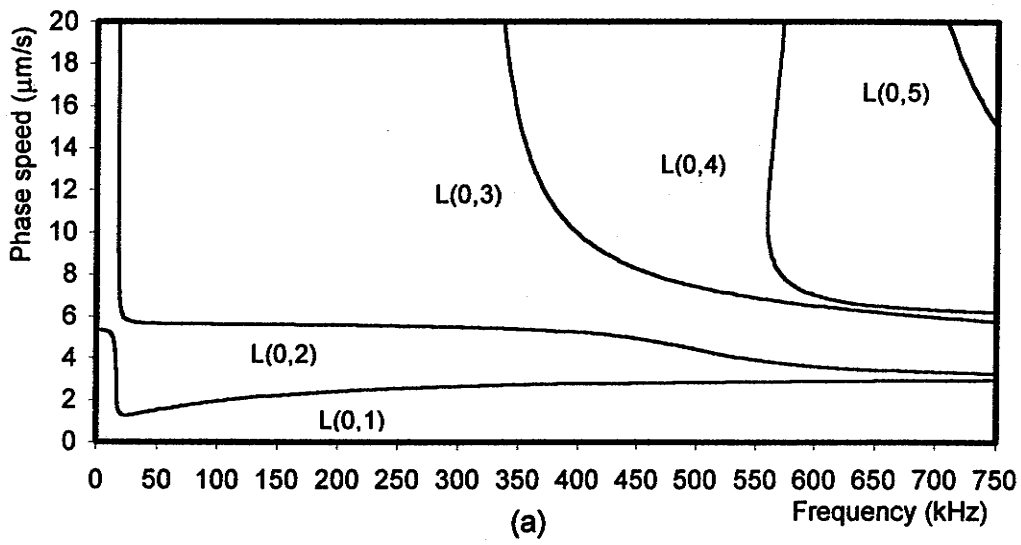

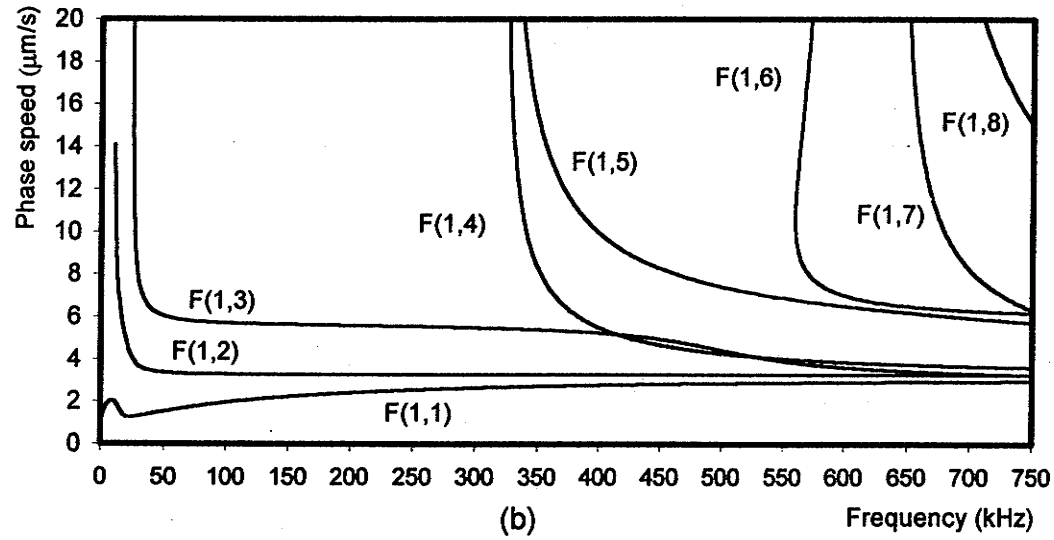

Figure 2.5. Phase speed as a function of frequency for a steel pipe. H/R=0.1 and ν=0.29. (a) Longitudinal wave (m=0), and (b) flexural wave (m=1)

Chapter 3

Hybrid Modeling of 3D Wave Scattering

Wave scattering happens when an incident wave strikes a crack or an irregularity. The scattered field carries substantial information about the location, size and shape of the scatterer. However, there are few publications giving theoretical data for elastic wave scattering by a crack in a cylinder. This is mainly because of the geometric and computational complexity of the problem. Most existing theoretical work has been confined to the axisymmetric case, (Rattanawangcharoen *et al.* 1997 and Zhuang *et al.* 1997). Only recently, Bai *et al.* (2001) studied 3D wave scattering by cracks in cylinders. However, the technique can not be applied to arbitrarily oriented flaws (cracks or inclusions). These cases, on the other hand, can be handled efficiently by using the hybrid method. To the best of the author's knowledge the use of the hybrid method for 3D wave scattering in cylinders has not been reported.

The hybrid method is a technique that combines a finite element idealization of a bounded region containing the inhomogeneities and a wave function expansion in the exterior region. Continuity conditions for displacements and tractions are applied at discrete points on the common boundaries between the two regions. This results in a system of linear equations in the unknown wave function amplitudes. The solution gives the amplitudes which are used to obtain the reflection and transmission coefficients of the

scattered fields. Satisfaction of reciprocity and the principle of energy conservation are used to check the validity and accuracy of the results. It is worth mentioning here that any other numerical technique (e.g. the finite difference method) could be used in the bounded region instead of the finite element method. Similarly, integral equations, for example, could be used instead of a wave function expansion in the external region.

3.1 Mathematical Idealization of a Crack

Since the problem of elastic wave scattering will be formulated mathematically, it is of paramount importance to have a clear vision of the mathematical abstraction of cracks and crack-like flaws. By definition, *a crack is a two-dimensional surface of finite or infinite area located in the interior of an elastic solid* (Kraut 1976). According to the type of boundaries, cracks are generally divided into two types, *weak cracks* and *rigid cracks*. In the case of a weak crack the surfaces of the crack are assumed free of stress. In the case of a rigid crack, conversely, the void is considered filled with an absolutely rigid material. In the present work, results are presented only for a weak crack. However, the numerical procedure can be extended to rigid cracks by imposing zero displacement boundary conditions on a crack's surfaces.

It is very important to recognize that ideal and real cracks may differ substantially in their behavior. Such differences may be attributed to two factors; the loading conditions and the interaction between the crack surfaces (Kraut 1976). First, a cracked specimen may show different ultrasonic scattering characteristics depending on whether it is loaded or not. Second, a planar crack (i.e. a crack whose thickness is neglected and whose faces are assumed to occupy the same plane), although mathematically convenient, neglects interactions between its faces.

3.2 Description of the Problem

Scattering of time-harmonic waves by cracks in an infinitely long cylinder is considered. The cylinder may be composed of one linearly elastic isotropic layer or a

number of perfectly bonded concentric cylinders with distinct mechanical properties. A lateral section of the geometry is represented in Figure 3.1 where the cylinder's mean radius is R and its uniform thickness is H. The surfaces of the cylinder are assumed free of stress. The illustrated cylinder extends to infinity in the axial direction from both ends. All the flaws are assumed to be localized so that they can be bounded appropriately by two vertical boundaries B^+ and B^-, respectively, at $z = z^+$ and $z = z^-$ where z is the coordinate along the axis of the cylinder.

The incident wave is considered to be harmonic. It is taken to be a single mode propagating in the negative z-direction. The common factor $e^{-j\omega t}$ is suppressed in the following mathematical formulation for convenience. For the finite element mesh representing the bounded region, the only externally applied forces are those acting on the nodes located at the boundaries B^+ and B^-. The external forces vanish elsewhere. No constraints are imposed at any node.

3.3 Mathematical Formulation

3.3.1 An Overview

One aim of the following overview of the mathematical formulation is to underscore the physics of the hybrid model. Consider a cylinder having flaws located between z^+ and z^-. Assume this cracked region to be a *"black box"*. The black box represents an obstacle to the propagating incident mode (p,q) excited at $-\infty$ and travelling to the left. To the left and right of the obstacle there will be incident and transmitted wave fields. Since the material of the cylinder is assumed linearly elastic, the principle of superposition applies, i.e. displacements and forces external to the obstacle can be determined by summing a finite number of normal modes of the undamaged cylinder. These forces and displacements represent the boundary conditions imposed on the bounded region.

The bounded region, which may contain geometric and/or material irregularities, is handled best numerically. The finite element procedure was chosen in the present formulation. Recall that other numerical techniques, e.g. the finite difference method, may be used instead. The end result of a numerical method is a system of algebraic equations with complex coefficients. The unknown variables are the complex amplitudes of the reflected and transmitted wave modes. These amplitudes represent the *"footprint"* (i.e. the location, shape, size, and orientation) of the crack.

3.3.2 Wave Function Expansion

Consider an incident wave mode (p,q) that corresponds to a wavenumber p in the θ-direction and a wavenumber ξ_{pq}^{I} in the z-direction. Upon striking the crack at $z=0$, a scattered field is generated. Using a wave-function expansion, the displacement vector of the scattered field can be written on the boundaries B^{+} and B^{-} as:

$$\boldsymbol{U}_B^{S\pm} = \sum_{-M}^{+M} \sum_{1}^{N_m} a_{mn}^{\pm} \boldsymbol{U}_{mn}^{\pm} e^{jm\theta} e^{j\xi_{mn} z^{\pm}} \tag{3.1}$$

where superscript "S" refers to the scattered field. Moreover, a "+" superscript refers to B^{+} and superscript "–" refers to B^{-}. M is the number of circumferential wavenumbers; N_m is the number of axial modes corresponding to a particular m; a_{mn} is the unknown complex amplitude of the (m,n) scattered mode; and

$$\boldsymbol{U}_{mn} = \frac{1}{g_{mn}} \left[u_{1mn}^{r} \quad u_{1mn}^{\theta} \quad u_{1mn}^{z} \quad \ldots u_{imn}^{r} \quad u_{imn}^{\theta} \quad u_{imn}^{z} \quad \ldots u_{N_B mn}^{r} \quad u_{N_B mn}^{\theta} \quad u_{N_B mn}^{z} \right] \tag{3.2}$$

where

$$g_{mn} = \sqrt{\sum_{i=1}^{N_B} \left(\left| u_{imn}^{r} \right|^2 + \left| u_{imn}^{\theta} \right|^2 + \left| u_{imn}^{z} \right|^2 \right)}. \tag{3.3}$$

The u^r_{imn}, u^θ_{imn} and u^z_{imn} are the displacement components in the r, θ and z directions, respectively, at the ith nodal point. They correspond to the (m,n)th mode. N_B is the (identical) number of nodal points on each boundary, B^+ and B^-. Equation (3.1) can be rewritten in matrix form as:

$$\boldsymbol{U}_B^{S\pm} = \boldsymbol{G}^{\pm}\boldsymbol{A}^{\pm} \tag{3.4}$$

The matrices on the right side of equation (3.4) are defined as:

$$\boldsymbol{G}^{\pm} = \left(\boldsymbol{U}^{\pm}_{-M1} \;..\; \boldsymbol{U}^{\pm}_{-MN_M} .. \; \boldsymbol{U}^{\pm}_{-11} \;..\; \boldsymbol{U}^{\pm}_{-1N_1} \boldsymbol{U}^{\pm}_{01} \;..\; \boldsymbol{U}^{\pm}_{0N_1} \;..\; \boldsymbol{U}^{\pm}_{i1} \;..\; \boldsymbol{U}^{\pm}_{iN_i} \;..\; \boldsymbol{U}^{\pm}_{M1} \;..\; \boldsymbol{U}^{\pm}_{MN_M}\right) \tag{3.5}$$

$$\boldsymbol{A}^{\pm} = \left(\bar{a}^{\pm}_{-M1} \;..\; \bar{a}^{\pm}_{-MN_M} \;..\; \bar{a}^{\pm}_{-11} \;..\; \bar{a}^{\pm}_{-1N_1} \bar{a}^{\pm}_{01} \;..\; .. \; \bar{a}^{\pm}_{0N_0} \; \bar{a}^{\pm}_{11} \;..\; .. \; \bar{a}^{\pm}_{1N_1} \;..\; \bar{a}^{\pm}_{M1} \;..\; .. \; \bar{a}^{\pm}_{MN_M}\right)^T \tag{3.6}$$

where

$$\bar{a}^{\pm}_{mn} = a^{\pm}_{mn} \exp\left(j\xi_{mn} z^{\pm}\right) \quad . \tag{3.7}$$

Similarly, the force vectors at the boundaries B^+ and B^- due to the scattered field can be written as:

$$\boldsymbol{P}_B^{S\pm} = \boldsymbol{F}^{\pm}\boldsymbol{A}^{\pm} \tag{3.8}$$

where

$$\boldsymbol{F}^{\pm} = \left(\boldsymbol{P}^{\pm}_{-M1} \;..\; \boldsymbol{P}^{\pm}_{-MN_M} .. \; \boldsymbol{P}^{\pm}_{-11} \;..\; \boldsymbol{P}^{\pm}_{-1N_1} \boldsymbol{P}^{\pm}_{01} \;..\; \boldsymbol{P}^{\pm}_{0N_1} \;..\; \boldsymbol{P}^{\pm}_{i1} \;..\; \boldsymbol{P}^{\pm}_{iN_i} \;..\; \boldsymbol{P}^{\pm}_{M1} \;..\; \boldsymbol{P}^{\pm}_{MN_M}\right) \tag{3.9}$$

and

$$\boldsymbol{P}_{mn} = \frac{1}{g_{mn}}\left[\, p^r_{1mn} \quad p^\theta_{1mn} \quad p^z_{1mn} \quad \cdots p^r_{imn} \quad p^\theta_{imn} \quad p^z_{imn} \quad \cdots p^r_{N_Bmn} \quad p^\theta_{N_Bmn} \quad p^z_{N_Bmn}\right]. \tag{3.10}$$

The p^r_{imn}, p^θ_{imn} and p^z_{imn} are the force components in the r, θ and z directions that correspond to the mode (m,n) at the ith nodal point. In constructing the load vector, the consistent load vector formulation (Bathé 1982 and Zienkiewicz 1977) is used. It can be

shown (see *Appendix B*) that $\boldsymbol{G}^-$ can be obtained from $\boldsymbol{G}^+$ by replacing the z-component of a displacement with its negative value. Similarly $\boldsymbol{F}^-$ can be obtained from $\boldsymbol{F}^+$ by replacing the z-component of a force with its negative value.

The boundary displacement and force vectors can be constructed for the incident wave as:

$$\boldsymbol{U}_B^{I-} = a_{pq}^I \boldsymbol{G}_{pq}^- \exp\left(-j\xi_{pq} z^-\right) \tag{3.11a}$$

$$\boldsymbol{U}_B^{I+} = a_{pq}^I \boldsymbol{G}_{pq}^- \exp\left(-j\xi_{pq} z^+\right) \tag{3.11b}$$

$$\boldsymbol{P}_B^{I-} = a_{pq}^I \boldsymbol{F}_{pq}^- \exp\left(-j\xi_{pq} z^-\right) \tag{3.11c}$$

$$\boldsymbol{P}_B^{I+} = -a_{pq}^I \boldsymbol{F}_{pq}^- \exp\left(-j\xi_{pq} z^+\right). \tag{3.11d}$$

where a *"I"* superscript indicates the incident wave field. $\boldsymbol{G}_{pq}^{\pm}$ and $\boldsymbol{F}_{pq}^{\pm}$ are the column of the $\boldsymbol{G}^{\pm}$ and $\boldsymbol{F}^{\pm}$ matrices corresponding to the incident mode (p,q) and a_{pq}^I is the amplitude of the incident mode (p,q).

3.3.3 Finite Element Idealization

The bounded region that contains the crack is idealized by using finite elements (Bathé 1982 and Zienkiewicz 1977). A 20-node (quadratic) brick element is used throughout the entire mesh. (For the same number of degrees of freedom, this element gives higher accuracy than an 8-node brick element (Kardestuncer 1987). Moreover a brick elment with more than 20 nodes incurs more computational effort with no gaurantee of better accuracy.) The displacement vector, $\boldsymbol{U}$, at any point within the element "e" requires the interpolation of the nodal displacement vector $\boldsymbol{Q}_e$. Indeed

$$\boldsymbol{U} = \boldsymbol{N}\boldsymbol{Q}_e \tag{3.12a}$$

where $\boldsymbol{N}$ is a matrix containing the interpolation (shape) functions. (See *Appendix C.*) Hence, for the 20-node brick element,

$$\boldsymbol{N} = \begin{bmatrix} n_1 & 0 & 0 & n_2 & 0 & 0 & \cdots & n_{20} & 0 & 0 \\ 0 & n_1 & 0 & 0 & n_2 & 0 & \cdots & 0 & n_{20} & 0 \\ 0 & 0 & n_1 & 0 & 0 & n_2 & \cdots & 0 & 0 & n_{20} \end{bmatrix}. \tag{3.12b}$$

Then the strain vector, ε, is given in terms of the displacement by:

$$\varepsilon = \left\langle \varepsilon^{rr} \quad \varepsilon^{\theta\theta} \quad \varepsilon^{zz} \quad \gamma^{z\theta} \quad \gamma^{zr} \quad \gamma^{r\theta} \right\rangle^T = \boldsymbol{DU} \tag{3.13a}$$

in which $\boldsymbol{D}$ is a matrix of differential operators that is given by:

$$\boldsymbol{D} = \begin{bmatrix} \dfrac{\partial}{\partial r} & 0 & 0 \\ \dfrac{1}{r} & \dfrac{1}{r}\left(\dfrac{\partial}{\partial \theta}\right) & 0 \\ 0 & 0 & \dfrac{\partial}{\partial z} \\ 0 & \left(\dfrac{\partial}{\partial z}\right) & \dfrac{1}{r}\left(\dfrac{\partial}{\partial \theta}\right) \\ \dfrac{\partial}{\partial z} & 0 & \left(\dfrac{\partial}{\partial r}\right) \\ \dfrac{1}{r}\left(\dfrac{\partial}{\partial \theta}\right) & \dfrac{\partial}{\partial r} - \dfrac{1}{r} & 0 \end{bmatrix}. \tag{3.13b}$$

By substituting the $\boldsymbol{U}$ given by equation (3.12a) into equation (3.13a), the corresponding strain vector, ε, can be written as:

$$\varepsilon = \boldsymbol{B_e Q_e} \tag{3.14}$$

where

$$\boldsymbol{B}_e = \boldsymbol{DN}\,. \tag{3.15}$$

The strain energy of the crack region is:

$$V = \frac{1}{2}\int_{\mathbb{R}} \bar{\varepsilon}^T \boldsymbol{C}\varepsilon d\mathbb{R} \tag{3.16a}$$

where an overbar refers again to a complex conjugate. $\boldsymbol{C}$ is the elasticity matrix given, for an isotropic material, by equation (2.7); while for an orthotropic material it takes the form:

$$\boldsymbol{C} = \begin{bmatrix} C_{11} & C_{12} & C_{13} & 0 & 0 & 0 \\ C_{12} & C_{22} & C_{23} & 0 & 0 & 0 \\ C_{13} & C_{23} & C_{33} & 0 & 0 & 0 \\ 0 & 0 & 0 & C_{44} & 0 & 0 \\ 0 & 0 & 0 & 0 & C_{55} & 0 \\ 0 & 0 & 0 & 0 & 0 & C_{66} \end{bmatrix}. \tag{3.16b}$$

In terms of the finite element idealization, equation (3.16) can be rewritten as,

$$V = \frac{1}{2}\sum_{1}^{N_e}\int_{\mathbb{R}_e} \bar{\varepsilon}^T \boldsymbol{C}\varepsilon d\mathbb{R}_e \tag{3.17}$$

where N_e is the number of elements and $\mathbb{R}_e$ is the element domain (volume). Similarly, the kinetic energy of the crack region is:

$$T = \frac{1}{2}\omega^2 \int_{\mathbb{R}} \rho \bar{\boldsymbol{U}}^T \boldsymbol{U} d\mathbb{R}\,. \tag{3.18}$$

which can be rewritten for the finite element idealization as:

$$T = \frac{1}{2}\omega^2 \sum_{1}^{N_e} \int_{\mathbb{R}_e} \rho \bar{\boldsymbol{U}}^T \boldsymbol{U} d\mathbb{R}_e . \tag{3.19}$$

The virtual work exerted on the crack region by the external forces is:

$$W = \frac{1}{2}\left\{ \bar{\boldsymbol{U}}_B{}^T \boldsymbol{P}_B + \boldsymbol{U}_B{}^T \bar{\boldsymbol{P}}_B \right\}. \tag{3.20}$$

A conventional assembly over the elements gives the total energy of the region, $E_{\mathbb{R}}$, as:

$$E_{\mathbb{R}} = V - T - W = \frac{1}{2}\left\{ \sum_{1}^{N_e} \left[\int_{\mathbb{R}_e} \left(\bar{\boldsymbol{\varepsilon}}^T \boldsymbol{C} \boldsymbol{\varepsilon} - \rho\omega^2 \bar{\boldsymbol{U}}^T \bar{\boldsymbol{U}} \right) d\mathbb{R}_e \right] - \bar{\boldsymbol{U}}_B{}^T \boldsymbol{P}_B - \boldsymbol{U}_B{}^T \bar{\boldsymbol{P}}_B \right\}. \tag{3.21}$$

It is important to point out that the total energy of the finite element domain is independent of time, t, since $\overline{\exp(-j\omega t)}\exp(-j\omega t)$ is unity. In view of equations (3.12) through (3.15), $E_{\mathbb{R}}$ can be rewritten as:

$$E_{\mathbb{R}} = \frac{1}{2}\left\{ \bar{\boldsymbol{U}}_{\mathbb{R}}{}^T \boldsymbol{S} \boldsymbol{U}_{\mathbb{R}} - \bar{\boldsymbol{U}}_B{}^T \boldsymbol{P}_B - \boldsymbol{U}_B{}^T \bar{\boldsymbol{P}}_B \right\} \tag{3.22}$$

where

$$\boldsymbol{U}_{\mathbb{R}}{}^T = \left\langle \boldsymbol{U}_I{}^T \quad \boldsymbol{U}_B{}^T \right\rangle \tag{3.23a}$$

and

$$\boldsymbol{S} = \boldsymbol{K} - \omega^2 \boldsymbol{M} = \begin{bmatrix} \boldsymbol{S}_{II} & \boldsymbol{S}_{IB} \\ \boldsymbol{S}_{BI} & \boldsymbol{S}_{BB} \end{bmatrix}. \tag{3.23b}$$

A subscript "*I*" refers to the degrees of freedom associated with the internal nodes in the finite element mesh; subscript "*B*", on the other hand, refers to the degrees of freedom associated with the boundary nodes. $\boldsymbol{K}$ and $\boldsymbol{M}$ are global stiffness and mass matrices, respectively. They are defined as:

$$\boldsymbol{K} = \sum_{1}^{N_e} \int_{\mathbb{R}_e} \boldsymbol{B}_e^T \boldsymbol{C} \boldsymbol{B}_e d\mathbb{R}_e \tag{3.24c}$$

and

$$\boldsymbol{M} = \sum_{1}^{N_e} \int_{\mathbb{R}_e} \rho \boldsymbol{N}^T \boldsymbol{N} d\mathbb{R}_e . \tag{3.24d}$$

Minimizing the total energy given by equation (3.22), results in the following equation of motion for the interior region (Bathé 1982 and Zienkiewicz 1977):

$$\delta E_{\mathbb{R}} = \delta \bar{\boldsymbol{U}}_{\mathbb{R}}{}^T \boldsymbol{S} \boldsymbol{U}_{\mathbb{R}} - \delta \bar{\boldsymbol{U}}_B{}^T \boldsymbol{P}_B = 0 . \tag{3.25}$$

δ implies a first variation and an overbar denotes the complex conjugate.

3.3.4 General Solution

The general solution is obtained by applying the displacement and force continuity conditions at the common boundaries B^+ and B^- between the internal and external regions, as follows:

$$\boldsymbol{U}_B = \boldsymbol{U}_B^I + \boldsymbol{U}_B^S \tag{3.26a}$$

$$\boldsymbol{P}_B = \boldsymbol{P}_B^I + \boldsymbol{P}_B^S \tag{3.26b}$$

where

$$\boldsymbol{U}_B^{I,T} = \left\langle \boldsymbol{U}_B^{I-,T} \quad \boldsymbol{U}_B^{I+,T} \right\rangle \tag{3.27a}$$

$$\boldsymbol{U}_B^{S,T} = \left\langle \boldsymbol{U}_B^{S-,T} \quad \boldsymbol{U}_B^{S+,T} \right\rangle \tag{3.27b}$$

$$\boldsymbol{P}_B^{I,T} = \left\langle \boldsymbol{P}_B^{I-,T} \quad \boldsymbol{P}_B^{I+,T} \right\rangle \tag{3.27c}$$

$$\boldsymbol{P}_B^{S,T} = \left\langle \boldsymbol{P}_B^{S-,T} \quad \boldsymbol{P}_B^{S-,T} \right\rangle. \tag{3.27d}$$

In equation (3.26), quantities on the left side of the equality are associated with the interior region while those on the right side correspond to the exterior region. Using equations (3.4) and (3.11) in equation (3.26) and, in turn, in equation (3.25) results in:

$$\boldsymbol{S}_{II}\boldsymbol{U}_I + \boldsymbol{S}_{IB}\boldsymbol{U}_B = 0 \tag{3.28a}$$

$$\boldsymbol{G}^T\left(\boldsymbol{S}_{BI}\boldsymbol{U}_I + \boldsymbol{S}_{BB}\boldsymbol{U}_B\right) = \boldsymbol{G}^T\boldsymbol{P}_B \tag{3.28b}$$

where the $\boldsymbol{S}_{ij}$ $(i, j = I, B)$ are defined in equation (3.23b) and

$$\boldsymbol{G} = \begin{bmatrix} \boldsymbol{G}^- & 0 \\ 0 & \boldsymbol{G}^+ \end{bmatrix}. \tag{3.28c}$$

$\boldsymbol{G}^-$ and $\boldsymbol{G}^+$ are defined in equation (3.5). Equation (3.28a) gives:

$$\boldsymbol{U}_I = -\boldsymbol{S}_{II}^{-1}\boldsymbol{S}_{IB}\boldsymbol{U}_B. \tag{3.29}$$

Substituting equation (3.29) in equation (3.28b) and making use of equation (3.26) leads to:

$$\left[\boldsymbol{G}^T\left(\boldsymbol{S}_{BB}^*\boldsymbol{G} - \boldsymbol{F}\right)\right]\boldsymbol{A} = \boldsymbol{G}^T\left(\boldsymbol{P}_B^I - \boldsymbol{S}_{BB}^*\boldsymbol{U}_B^I\right) \tag{3.30}$$

in which,

$$\boldsymbol{S}_{BB}^* = \boldsymbol{S}_{BB} - \boldsymbol{S}_{BI}\boldsymbol{S}_{II}^{-1}\boldsymbol{S}_{IB}, \tag{3.31}$$

$$\boldsymbol{A} = \left\langle \boldsymbol{A}^- \quad \boldsymbol{A}^+ \right\rangle \tag{3.32}$$

and

$$F = \begin{bmatrix} F^- & 0 \\ 0 & F^+ \end{bmatrix}, \tag{3.33}$$

where F^- and F^+ are defined by equations (3.9) and (3.10). The size of the matrix of coefficients in equation (3.30) is $2N_T$ by $2N_T$ where N_T is the total number of modes taken in the wave function expansion. The amplitudes $a_{mn}^{\pm}$ are obtained by solving the linear equation (3.30) for A^+ and A^-, making use of (3.7). The U_B, whose overall form is given by equation (3.4), is computed from equation (3.26) while U_I is given by equation (3.29).

The reflection coefficients $R_{pq,mn}$ of the (m,n) reflected mode and the transmission coefficient $T_{pq,mn}$ of the (m,n) transmitted mode, due to the (p,q) incident mode, are defined as:

$$R_{pq,mn} = \frac{a_{mn}^{+}}{a_{pq}^{I}} \tag{3.34a}$$

and

$$T_{pq,mn} = \begin{cases} \dfrac{a_{mn}^{-}}{a_{pq}^{I}} & m \neq p \text{ or } n \neq q \\ \dfrac{a_{pq}^{I} + a_{mn}^{-}}{a_{pq}^{I}} & m = p \text{ and } n = q. \end{cases} \tag{3.34b}$$

3.3.5 Principle of Energy Conservation

Reflected and transmitted energy is carried far from the crack by the propagating modes. The time-averaged value of the energy flux associated with the (m,n) mode propagating through the cylinder, that is due to the (p,q) incident mode, is given by (Karunasena 1992):

$$\Phi^{+}_{pq,mn} = \omega \left| a^{I}_{pq} \right|^2 \left| R_{pq,mn} \right|^2 \Psi_{mn} \tag{3.35}$$

where

$$\Psi_{mn} = \mathrm{Im}\left(F^{+,T}_{mn} \bar{U}^{+}_{mn} \right) \qquad 1 \le n \le N_{pr} . \tag{3.36}$$

The N_{pr} represents the number of propagating modes in the axial direction. The energy flux of the (m,n) transmitted mode and the (p,q) incident wave can be written respectively as:

$$\Phi^{-}_{pq,mn} = \omega \left| a^{I}_{pq} \right|^2 \left| T_{pq,mn} \right|^2 \Psi_{mn} \tag{3.37a}$$

$$\Phi^{I}_{pq} = \omega \left| a^{I}_{pq} \right|^2 \Psi_{pq} . \tag{3.37b}$$

The percentage error in the energy balance, e, is defined as:

$$e = \frac{100}{\Phi^{I}_{pq}} \left[\Phi^{I}_{pq} - \sum_{-M}^{M} \sum_{n=1}^{N_{pr}} \left(\Phi^{+}_{pq,mn} + \Phi^{-}_{pq,mn} \right) \right] . \tag{3.38}$$

Application of the principle of conservation of energy to the closed region $\mathbb{R}$, which is bounded by $z = z^{-}$ and $z = z^{+}$, and the outer and inner surfaces of the cylinder is used to assess the accuracy of the numerical computations.

3.3.6 Reciprocal Relations

Application of the elastodynamic reciprocity theorem (Achenbach 1973; Auld 1973 and Tan and Auld 1980) to region $\mathbb{R}$ results in (Karunasena 1992 and Karunasena *et al.* 1991):

$$R_{pq,mn} \Upsilon_{mn} = R_{mn,pq} \Upsilon_{pq} \tag{3.39a}$$

$$T_{pq,mn} \Upsilon_{mn} = T_{mn,pq} \Upsilon_{pq} . \tag{3.39b}$$

Υ_{mn} is related to Ψ_{mn} by:

$$\Upsilon_{mn} = 2j\Psi_{mn}. \tag{3.40}$$

Let $E^{+}_{pq,mn}$ be the proportion of the energy of the incident (p,q) mode transferred to the (m,n) reflected mode. Then, from equations (3.35) and (3.37b),

$$E^{+}_{pq,mn} = \frac{\Phi^{+}_{pq,mn}}{\Phi^{I}_{pq}} = \left|R_{pq,mn}\right|^2 \frac{\Psi_{mn}}{\Psi_{pq}} \tag{3.41}$$

and,

$$E^{+}_{mn,pq} = \frac{\Phi^{+}_{mn,pq}}{\Phi^{I}_{mn}} = \left|R_{mn,pq}\right|^2 \frac{\Psi_{pq}}{\Psi_{mn}}. \tag{3.42}$$

Equation (3.39) and equations (3.40) through (3.42) lead to:

$$E^{+}_{pq,mn} = E^{+}_{mn,pq}. \tag{3.43}$$

Similarly, it can be shown, for the transmitted modes, that:

$$E^{-}_{pq,mn} = E^{-}_{mn,pq}. \tag{3.44}$$

The reciprocity relations given in equations (3.39), (3.43) and (3.44) serve as another useful check of the numerical computations.

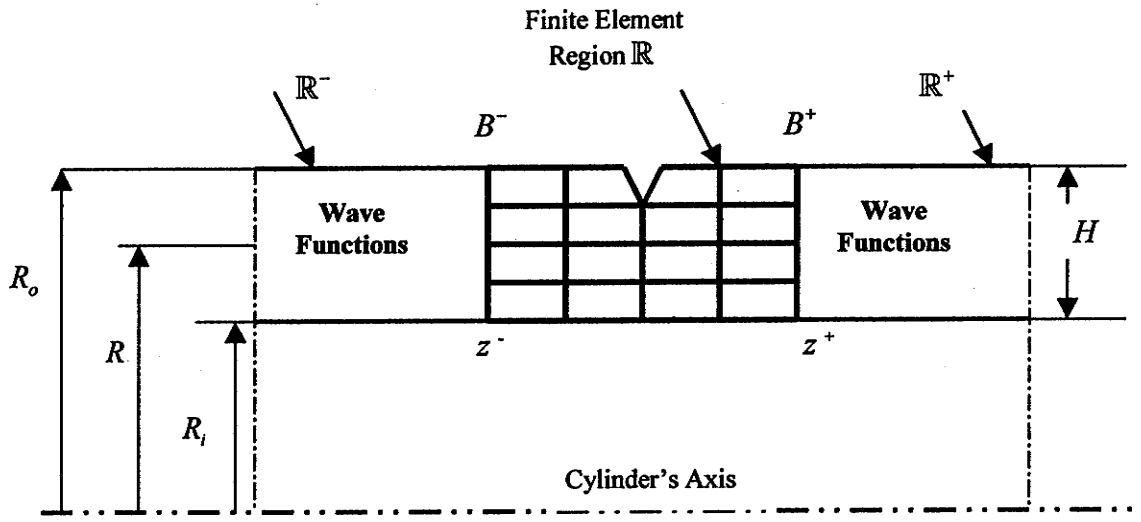

Figure 3.1. Lateral section in a cylinder having a surface breaking, symmetrical crack

Chapter 4

Numerical Implementation

The numerical implementation of the hybrid method for three dimensional problems requires enormous computer storage due to the imperative need for a refined finite element mesh in the bounded region. This obstacle has been circumvented in the following numerical implementation by using a condensation technique in which the stiffness matrix of the entire mesh is divided into smaller sized submatrices. Moreover, the condensation requires not only less storage but also less computational time for a given problem.

4.1 Condensation Technique

The mesh adopted in the finite element region is chosen to suit the condensation procedure. The numbering of the global nodes starts at the point $(r=0,\theta=0,z=0)$. At any plane $z=const.$, and each increment in the $r-direction$, numbering starts at $\theta=0$ and proceeds in the positive $\theta-direction$, see Figure 2.1. The planes normal to the $z-direction$ are ordered in the following manner. First, the plane at $z=0$ is considered Plane 1. Then the adjacent two planes (on the negative and positive sides of the crack) are considered Plane 2 and so on.

The mathematical formulae of the condensation method are presented for the 20-node brick element. The number of planes perpendicular to the z-direction is assumed, for simplicity, to be four. An illustration of the meshing scheme for this configuration is shown in Figure 4.1. Now equation (3.25) can be rewritten, in conjunction with equation (3.23b), to take the form:

$$\begin{bmatrix} S_{11} & S_{12} & S_{13} & 0 & 0 \\ S_{12}^{T} & S_{22} & S_{23} & 0 & 0 \\ S_{13}^{T} & S_{23}^{T} & S_{33} & S_{34} & S_{3B} \\ 0 & 0 & S_{34}^{T} & S_{44} & S_{4B} \\ 0 & 0 & S_{3B}^{T} & S_{4B}^{T} & S_{BB} \end{bmatrix} \begin{Bmatrix} U_1 \\ U_2 \\ U_3 \\ U_4 \\ U_5 \end{Bmatrix} = \begin{Bmatrix} 0 \\ 0 \\ 0 \\ 0 \\ P_B \end{Bmatrix}. \tag{4.1}$$

The elimination of U_1, U_2 and U_3 is performed as follows:

$$U_1 = -S_{11}^{*\,-1}\left\{S_{12}^{*}U_2 + S_{13}^{*}U_3\right\} \tag{4.2a}$$

$$U_2 = -S_{22}^{*\,-1}S_{23}^{*}U_3 \tag{4.2b}$$

$$U_3 = -S_{33}^{*\,-1}\left\{S_{34}^{*}U_4 + S_{3B}^{*}U_B\right\} \tag{4.2c}$$

$$U_4 = -S_{44}^{*\,-1}S_{4B}^{*}U_B \tag{4.2d}$$

where S_{ij}^{*} are given more conveniently in *Appendix D*. This results in the following two simultaneous linear equations:

$$\begin{bmatrix} S_{44}^{*} & S_{4B}^{*} \\ S_{4B}^{*T} & S_{BB}^{*} \end{bmatrix} \begin{Bmatrix} U_4 \\ U_B \end{Bmatrix} = \begin{Bmatrix} 0 \\ P_B \end{Bmatrix}. \tag{4.3}$$

The *dynamic memory allocation capabilities* of *Fortran 90* (Schick and Silverman 1995), combined with the *directives* of *OpenMP* (Chandra *et al.* 2001), enable the numerical condensation scheme to be implemented on *parallel processing platforms*. The

use of four threads, each with a 700 *MHz* clock speed and a 1*GB* hard drive, saves 67% of the
CPU time compared with only one thread being employed. Increasing the number of threads from four does not necessarily reduce the computational time because of the corresponding increase in the time overhead for the parallel processing.

4.2 Numerical Procedure

The hybrid modeling has five major computational tasks. These tasks are:

1. pre-processing;
2. calculation of condensed finite element stiffness;
3. calculation of wave functions.;
4. forming the linear system; and
5. post-processing.

In the pre-processing phase, the finite element mesh and wave data are generated for the undamaged cylinder. The finite element mesh is used in the second phase to calculate the condensed stiffness matrix. Wave data are used in the third phase to compute the wave functions. The condensed stiffness is used in the fourth phase, in combination with the wave functions, to form a linear system of equations in the complex unknowns. In the post-processing phase, the equations are solved, complex amplitudes are evaluated and the error in the energy balance is determined.

4.3 Validation

Three *necessary* conditions must be met to primarily validate the numerical procedure (Karunasena *et al.* 1991 and Karunasena 1992). First, for an incident wave and no crack in the interior region, the resulting scattered field must disappear. Second, the percentage error in the energy balance must also vanish. Third, the elastodynamic

reciprocity relations must be satisfied. These conditions were successfully met with negligible error for the numerical results presented in the following section. A comparison of these results with previously and independently obtained, numerical and experimental data also validates the model.

4.4 Numerical Results and Discussion

In the upcoming examples considered in this section, the non-dimensional wavenumber and frequency are defined respectively as:

$$\Omega = \frac{\omega}{\omega_{ref}} \quad \text{and} \quad \gamma = \frac{\xi}{\xi_{ref}} \tag{4.4a}$$

where,

$$\omega_{ref} = \frac{1}{H}\sqrt{\frac{\mu}{\rho}} \quad \text{and} \quad \xi_{ref} = \frac{1}{H}. \tag{4.4b}$$

The crack's geometry is described by two parameters; *viz. the non-dimensional crack depth, D*, and *the non-dimensional crack length L.* D is given by,

$$D = \frac{d}{H} \tag{4.5}$$

where d is the crack depth and L is given by,

$$L = \frac{\theta_c}{2\pi}. \tag{4.6}$$

θ_c (rads) is the angle circumscribed at the center of the cylinder by radii passing through the two circumferential edges of the crack. Furthermore, the non-dimensional width, W, of the bounded region $\mathbb{R}$ is defined as:

$$W = \frac{w}{H} \tag{4.7}$$

where w is the width of $\mathbb{R}$, i.e. $w = z^+ - z^-$. If the cylinder is welded, the non-dimensional thickness of the weld is defined as:

$$B = \frac{b}{H} \tag{4.8}$$

where b is the weld's (constant) thickness.

Numerical results are presented for the following examples.

Example 4.1 A cylinder, investigated previously by Zhuang *et al.* (1997), has the geometric and material properties summarized in Table 2.1. Numerical results are presented for axisymmetric cracks having a non-dimensional crack depth, D, of 0.125, 0.25 and 0.5.

Example 4.2 The cylinder in the Example 4.1 is reconsidered. Numerical results are presented for two vertical cracks having a non-dimensional crack length, L, of 0.5 and 0.1 and a constant non-dimensional crack depth, D, of 0.5. A comparison is given with an axisymmetric crack having the same depth.

Example 4.3 The cylinder in the Example 4.1 is re-examined to study the variation of the reflection and transmission coefficients as the non-dimensional length of a crack is changed for a constant non-dimensional crack depth, D, of 0.5.

Example 4.4 A cylinder that has been investigated previously (Alleyne *et al.* 1998, Lowe *et al.* 1998 and Bai *et al.* 2001) is considered. It has the geometric and material properties summarized in Table 2.1. Numerical results are presented for three cracks having a non-dimensional crack length, L, of 0.1, 0.5 and 1 and a constant non-dimensional crack depth, D, of 0.55.

Example 4.5 The cylinder in Example 4.4 is reconsidered to assess the division of the reflected and transmitted energies between different modes. The crack has a non-dimensional crack depth, D, of 0.55 and a non-dimensional crack length, L, of 0.5.

Three key factors affect the numerical accuracy of the hybrid model; the sizing of the finite element mesh, the total number of modes used in the wave function expansion and the total number of sublayers. The finite element mesh refers to the number and distribution of elements in each coordinate direction. The number of modes refers implicitly to the number of circumferential and axial modes. The total number of sublayers, N_s, is taken such that a convergent value is obtained for the Ψ_{mn} given by equation (3.36). The percentage error in the energy balance guides the adequacy of a particular finite element mesh and the number of modes used in the wave function expansion.

Consider a cylinder having the geometric and material properties given in Table 2.1. The cylinder contains an axisymmetric crack corresponding to a non-dimensional depth, D=0.5. The incident wave is the longitudinal mode $L(0,2)$. Using 10 radial elements, the percentage error in the energy balance is as little as 0.093%. Increasing the number of radial elements from 10 to 50 decreases the percentage error in the energy balance to 0.008%. However, the corresponding reflection coefficient $|R_{02,02}|$ grows by

less than 2%. (See Figure 4.2.) Consequently, 10 radial elements are a reasonable compromise in the radial direction.

Consider the previous cracked cylinder but the incident wave is changed from $L(0,2)$ to $F(1,3)$. The number of radial elements is fixed at 10. Numerical accuracy depends now on the number of circumferential elements used. For 20 circumferential elements, the percentage error in the energy balance is around an acceptable 0.006%.

To determine the number of modes to be used in the wave function expansion, the numerical procedure was tested for a cylinder having the geometry and material data presented in Table 2.1. The cylinder contained a surface-breaking crack in the $z = 0$ plane. The non-dimensional crack depth and crack length were D=0.5 and L=0.5, respectively. The incident wave was the second longitudinal mode $L(0,2)$ with a frequency of $70\ kHz$. A plot of the percentage error in the energy balance is shown in Figure 4.3 for different numbers of modes used. This percentage error is around 0.006% for 957 modes. These modes include 37 axial modes corresponding to $m = 0$ and 46 axial modes that correspond to each m from ± 1 to ± 10. When the incident wave is the $F(1,3)$ rather than the $L(0,2)$ mode, the 957 modes in the wave function expansion give a somewhat larger 0.050% error in the energy balance which is still acceptable.

Example 4.1

Two steel pipes are welded edgewise by a vertical weldment, with a surface-breaking crack on one of the weldment's interfaces. The non-dimensional width, W, of the bounded region is 0.28 for a non-dimensional thickness of the weldment of 0.14. The thickness-to-mean radius ratio, H/R, and the total thickness, H, of the steel pipes are 0.1 and $5.08\ mm$, respectively. The cylinder's material in this example has a modulus of elasticity, E, and Poisson ratio, ν, of 211.7 GPa and 0.29 respectively. The longitudinal and torsional wave speeds are $c_p = 35.6\times10^3\ m/s$ and $c_s = 5.88\times10^3\ m/s$.

The geometrical data and material properties are summarized in Table 2.2. The weld material is orthotropic. Its properties are summarized in Table 4.1.

Figure 4.4 shows that the results from the 2D (Zhuang *et al.* 1997) and 3D hybrid models are identical except at the higher frequencies when the 3D hybrid model gives slightly lower predictions. The relatively fewer radial elements employed in the 3D model accounts for this difference. Besides serving as a validating test, this example also shows the sensitivity of the reflection coefficient, $R_{01,01}$, to a variation in the non-dimensional crack depth, D. (See Figure 4.4.)

Example 4.2

The geometric and material properties are identical to those used in Example 4.1. Results are presented in Figure 4.5 for two vertical cracks having non-dimensional lengths, L, of 0.5 and 0.1 and a constant non-dimensional crack depth, D, of 0.5. The corresponding axisymmetric curve is superimposed on Figure 4.5. A comparison of the three curves shows that the reflection coefficient $R_{01,01}$ is very sensitive to the variation of the non-dimensional crack length, L.

Example 4.3

The geometric and material properties of the cylinder considered in this example are the same as before. The non-dimensional crack depth, D, is 0.5. The reflection and transmission coefficients, $R_{01,mn}$ and $T_{01,mn}$ $(m=0, n=1,2)$ $(m=1, n=1..3)$, respectively, are shown in Figure 4.6 as a function of the non-dimensional crack length, L, for a frequency, f, of 190 *kHz*. It can be seen from this figure that the reflection coefficients, $|R_{01,01}|$ and $|R_{01,02}|$, and the corresponding transmission coefficients, $|T_{01,01}|$ and $|T_{01,02}|$, are nearly linear functions of L. However, the former increase with increasing L but the latter decrease.

Example 4.4

The modulus of elasticity, E, and Poisson's ratio, ν, of the cylinder's material are 216.9 GPa and 0.287, respectively. Hence, the longitudinal and torsional wave speeds are $c_p = 32.6\times10^3\ m/s$ and $c_s = 5.96\times10^3\ m/s$. The inner radius, R_i, and the thickness, H, of the cylinder are 38 mm and 5.5 mm respectively. Therefore, the thickness-to-mean radius ratio, H/R, is 0.135. The geometrical and material properties are summarized in Table 2.1.

The frequency and phase speed spectra of the incident waves have been discussed thoroughly in *Chapter 2*. See also Figures 2.2 and 2.3. Alleyne *et al.* (1998) and Bai *et al.* (2001) presented experimental and numerical results, respectively, for the frequency range from 60 to 85 kHz. The incident wave is the second longitudinal mode, $L(0,2)$. The crack's non-dimensional crack depth is D=0.5.

Three different crack configurations are considered. However, in all cases, the plane containing the crack is perpendicular to the axial direction, z. Furthermore, the non-dimensional crack depth, D, is always 0.5. In the first configuration, the non-dimensional crack length, L, is 1 so that the problem is axisymmetric. In the second and third configurations, the non-dimensional crack length, L, is changed to 0.5 and 0.1.

A comparison of the results from the 3D-hybrid model with those of Alleyne *et al.* (1998) and Bai *et al.* (2001) is shown in Figure 4.7. The results from the hybrid model are about 9% lower than the numerical predictions of Bai *et al.* (2001). This is attributable to the difference in the finite element idealizations. Bai *et al.* employed 10,000 circumferential elements while the present hybrid model uses only 20 such elements. As the number of elements increases, the finite element procedure predicts a larger displacement (Desai *et al.* 1972). Experimental data are also higher than that predicted by the 3D hybrid model. One or more of the following factors may account for this difference:

1. material imperfections;
2. poor coupling between the experimentally used sensors and the wall of the cylinder;
3. experimental error in measuring the crack depth.

Numerical experiments were conducted using the present numerical procedure to predict an adjustment factor for a given crack depth. It was found that, if the crack depth was adjusted by a factor of 1.125, the experimental and current numerical data fitted very closely. See, for instance, Figure 4.8. On the other hand, the adjustment for Bai's predictions was 1.1 rather than 1.125. Again, the different finite idealizations account for the discrepancy.

Example 4.5

The geometric and material properties are given in Example 4.4 The crack's non-dimensional depth and length are 0.55 and 0.5, respectively. The variations of the reflection and transmission coefficients are shown in Figures 4.8 and 4.9 for different modes. Clearly, the reflection and transmission coefficients have a very weak dependence on frequency. This feature would be attractive for ultrasonic measurements over long pipes.

Table 4.1. Properties of the weld material (Examples 4.1, 4.2 and 4.3)

PROPERTY	VALUE
$C_{11} = C_{22},\ Gpa$	231.83
$C_{33},\ Gpa$	265.23
$C_{12},\ GPa$	67.83
$C_{13} = C_{23},\ GPa$	161.97
$C_{44} = C_{55} = C_{66},\ Gpa$	82.00
$\rho,\ kg/m^3$	780.00

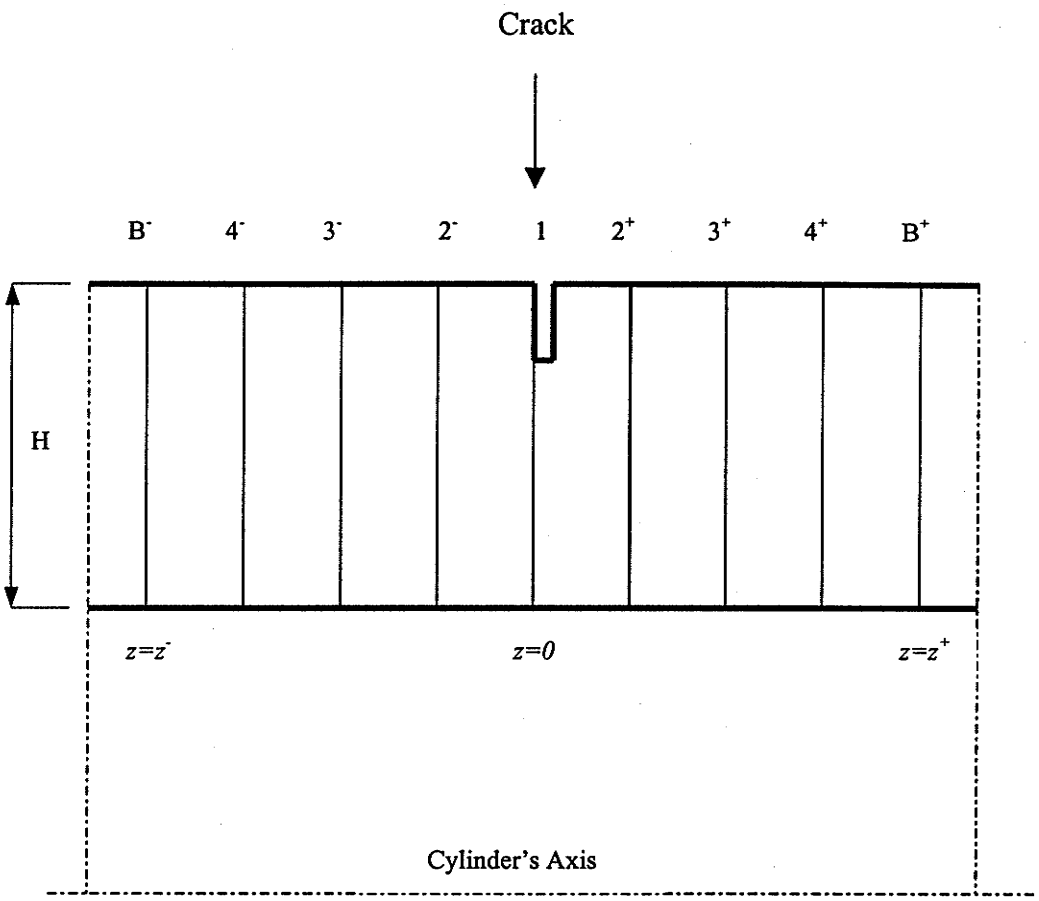

Figure 4.1. Illustration of the meshing scheme for the condensation procedure

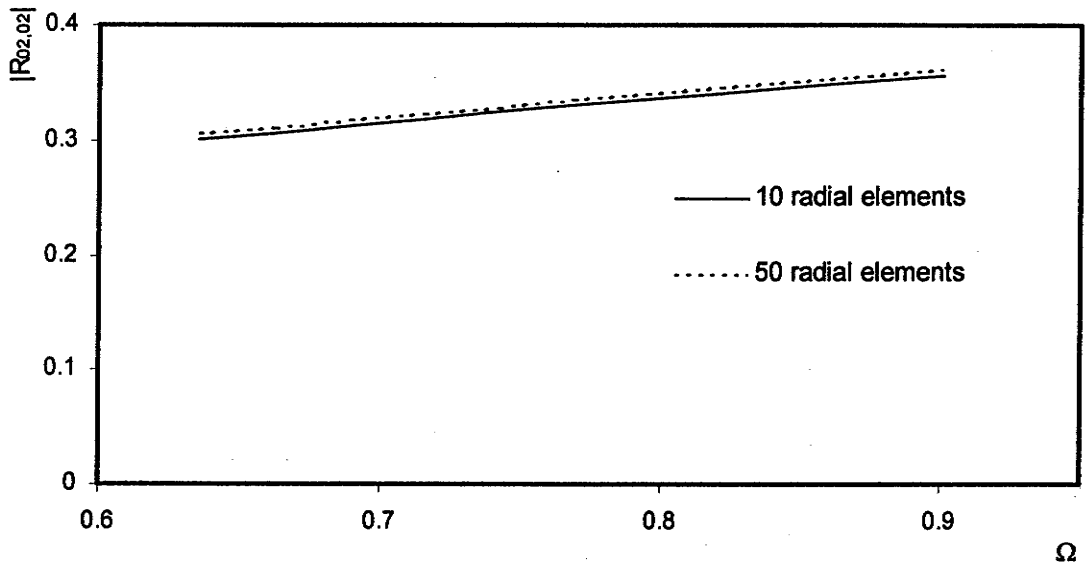

Figure 4.2. Variation of reflection coefficients with an increasing number of radial elements for a steel pipe. H/R=0.135, ν=0.287, D=0.5, L=1.0, W=0.2

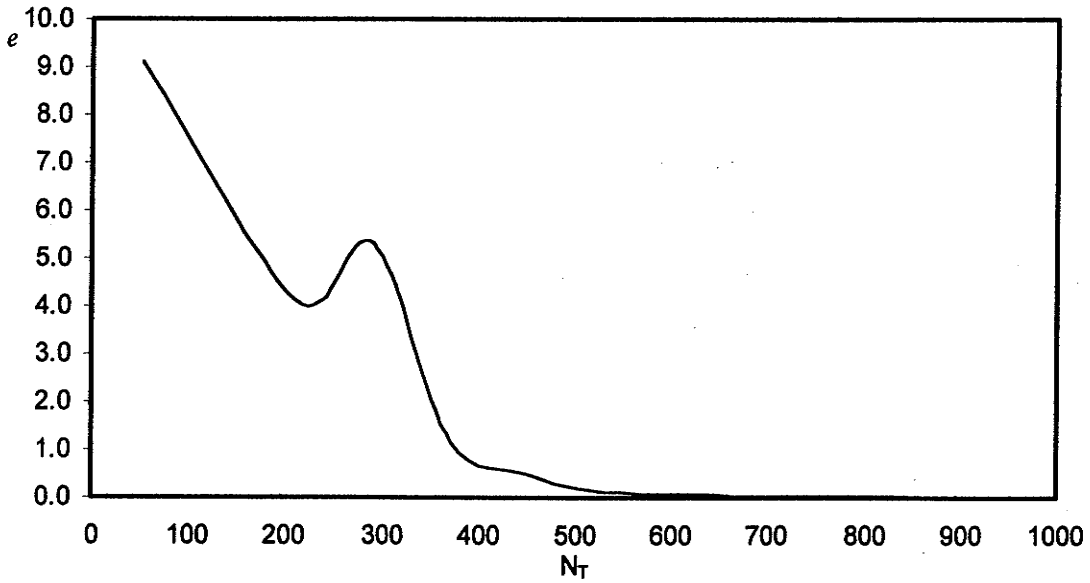

Figure 4.3. Percentage error in the energy balance versus the total number of modes used

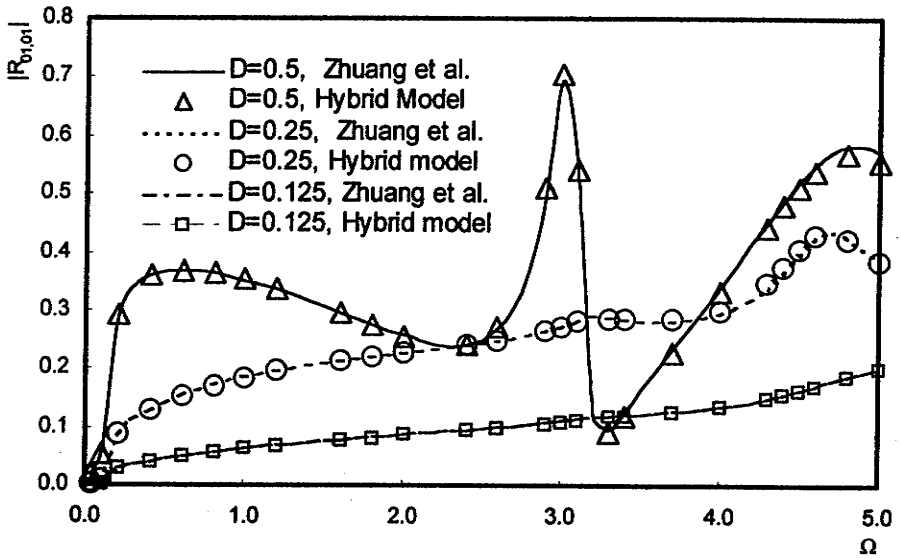

Figure 4.4. Reflection coefficients versus normalized frequency for various axisymmetric cracks in a welded steel pipe. H/R=0.1, ν=0.29, W=0.28, B=0.14

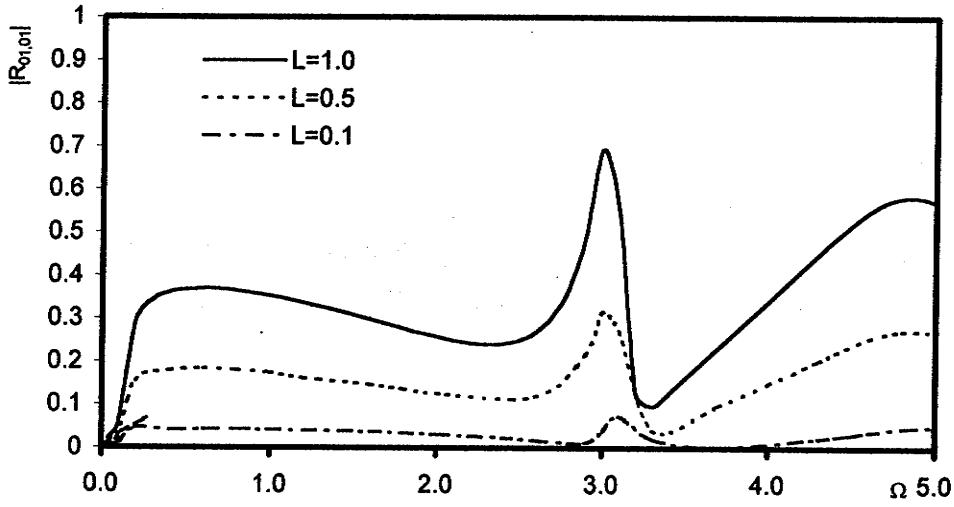

Figure 4.5. Reflection coefficients versus normalized frequency for various circumferential cracks in a welded steel pipe. H/R=0.1, ν=0.29, D=0.5, W=0.28, B=0.14

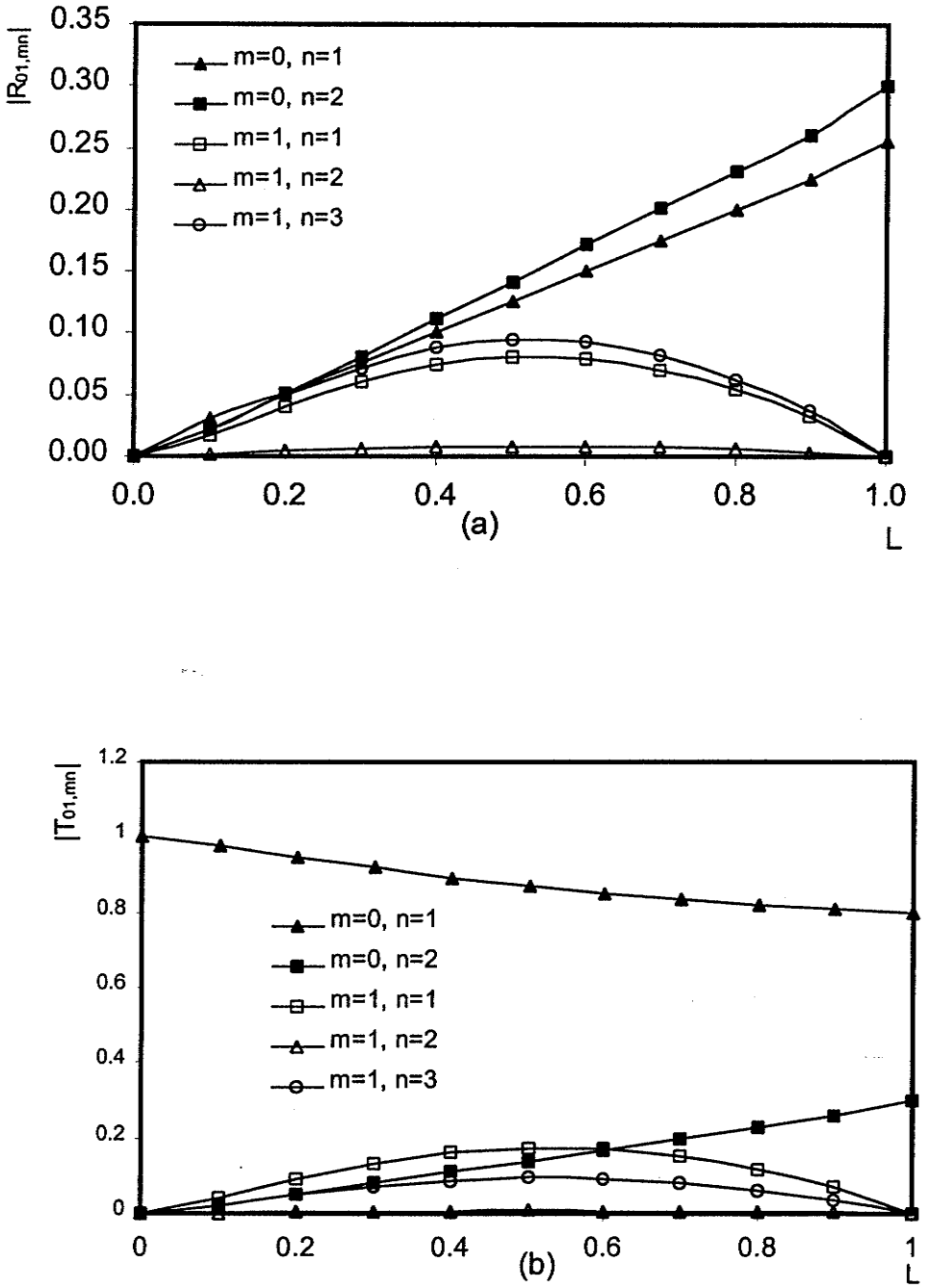

Figure 4.6. Normalized reflection and transmission coefficients in a welded steel pipe as a function of the crack length. f=190kHz, H/R=0.1, ν=0.29, D=0.5, W=0.28, B=0.14. (a) Reflection coefficients, and (b) transmission coefficients

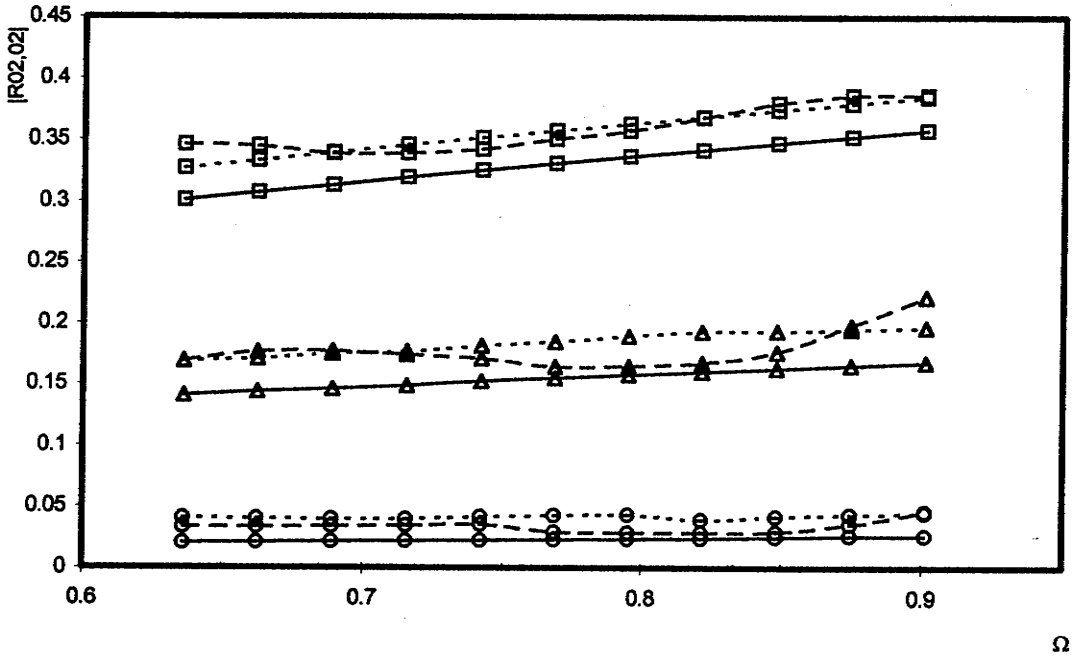

Figure 4.7. Reflection coefficients for three different crack lengths

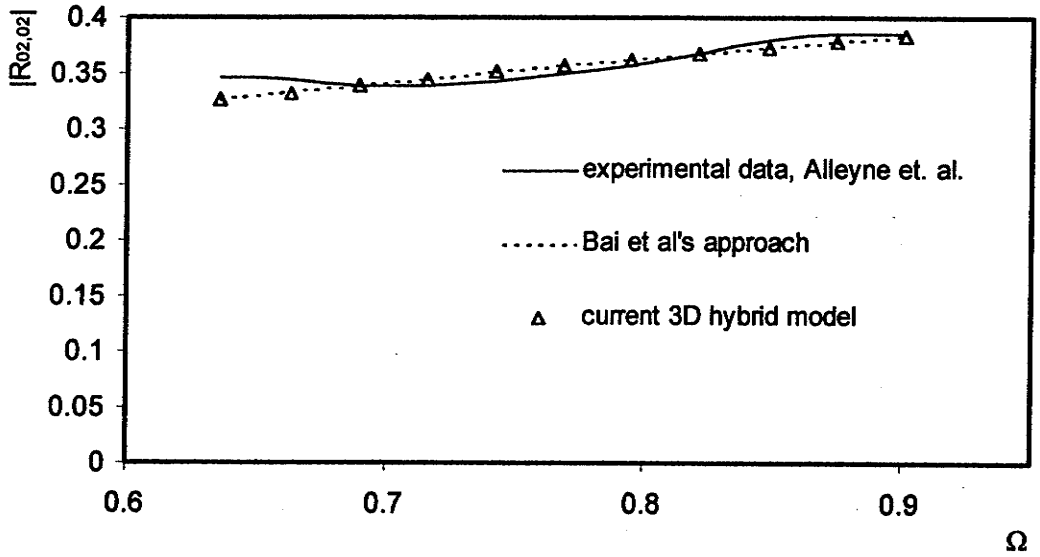

Figure 4.8. Reflection coefficients for an axisymmetric circumferential crack D=0.50 for continuous curve, D = 0.55 for dashed line, and D = 0.575 for triangles

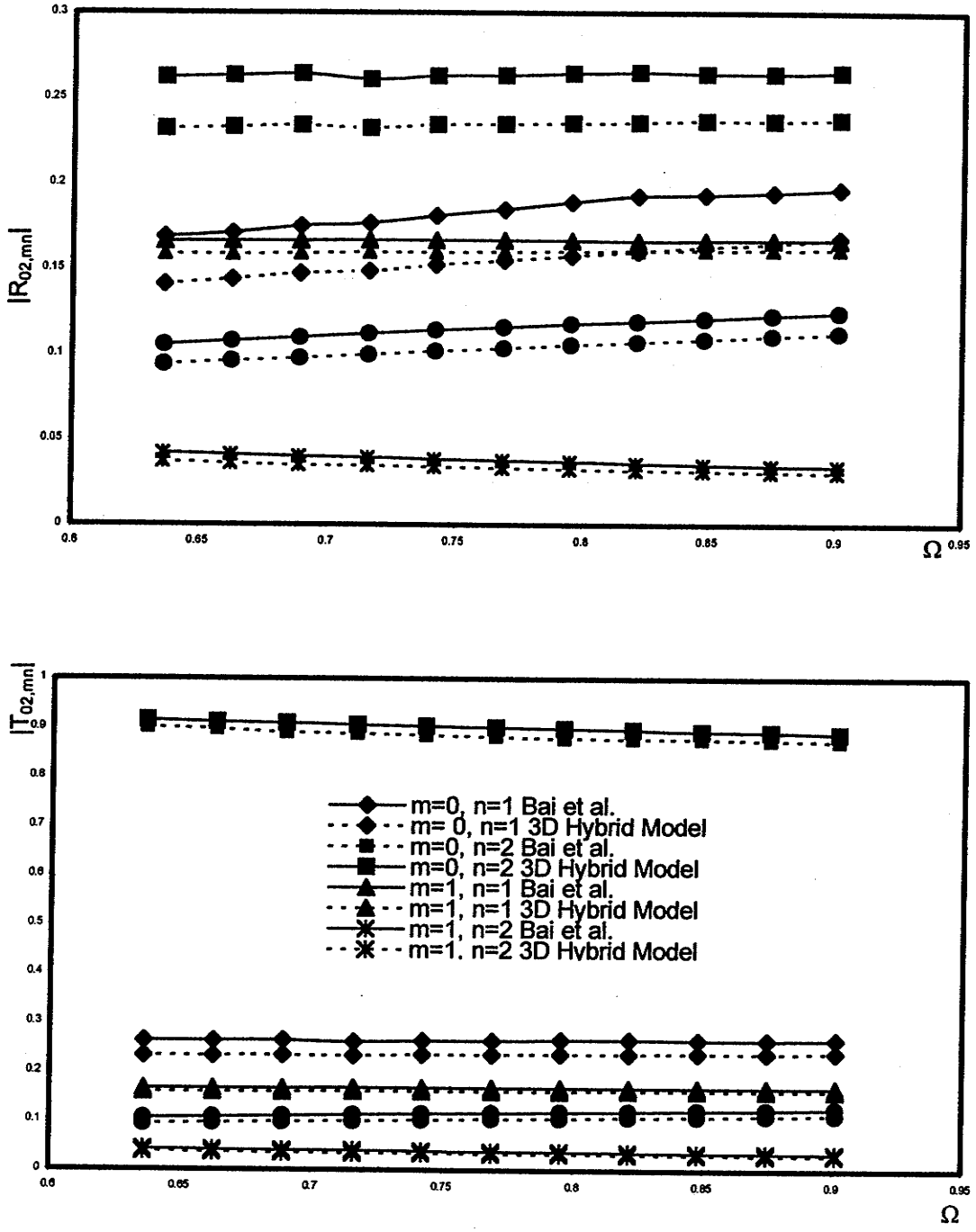

Figure 4.9. Normalized reflection and transmission coefficients in a steel pipe. H/R=0.135, ν=0.287, L=0.5, D=0.55, W=0.2. (a) Reflection coefficient, and (b) transmission coefficient

Chapter 5

Conclusions and Recommendations

5.1 Conclusions

In the present study a hybrid method, involving finite elements and a wave function expansion, was extended to analyze 3D scattering in a cracked circular cylinder. The implementation of the hybrid method was found to be hampered by its potentially tremendous computer storage requirements. The condensation technique outlined in *Chapter 4* partially solved this problem. *Fortran 90 dynamic memory allocation capabilities,* combined with *OpenMP directives*, also enabled the numerical condensation scheme to be implemented beneficially on a *parallel computer platform.*

Satisfaction of reciprocity and the principle of energy conservation were used to validate the numerical results. The results were also compared with available numerical and experimental data. Results from the current model and a previous 2D hybrid model are identical except at the highest frequencies. Then the current model gives very slightly lower values. The somewhat greater number of layers used in the 2D hybrid model probably accounts for this difference. The current model predicts somewhat lower values for the reflection and transmission coefficients compared with the quasi-exact method of

Bai *et al.* However the CPU time required by the current model is about 32 times that consumed by Bai *et al.*'s procedure for the same problem.

5.2 Recommendations For Future Work

The computational time can be reduced either by modifying the condensation procedure or by improving the parallel processing capability of the code. Dividing the overall finite element stiffness matrix into more but smaller sized sub-matrices may improve the condensation procedure's computational efficiency. Paralleling more segments in the code may enhance the parallel processing but radical changes would be needed in the present algorithm. The current 3D algorithm also lacks the ability to handle a non-uniform finite element mesh. Algorithmic modifications are required and numerical experiments are needed to determine the most appropriate non-uniform finite element mesh for m greater than zero.

References

Abduljabbar, Z., Datta, S. K., and Shah, A. H., 1983, "Diffraction of Horizontally Polarized Shear Waves by Normal Edge Cracks in a Plate," *Journal of Applied Physics*, **54**(4), pp. 461-472.

Achenbach, J. D., 1973. *Wave Propagation in Elastic Solids*. North-Holland Publishing Company, Amsterdam.

Alleyne, D. N., Lowe, M. J. S., and Cawley, P., 1998, "The Reflection of Guided Waves from Circumferential Notches in Pipes," ASME *Journal of Applied Mechanics,* **65,** pp. 635-641.

Armenàkas, A. E., 1967, "Propagation of Harmonic Waves in Composite Cylindrical Shells, Part I: Theoretical Investigation," AIAA *Journal*, **5**, pp. 740-744.

Armenàkas, A. E., 1971, "Propagation of Harmonic Waves in Composite Cylindrical Shells, Part II: Numerical Analysis," AIAA *Journal*, **9**, pp. 599-605.

Armenàkas, A. E., Gazis, D. C., and Hermann, G., 1969. *Free Vibration of Circular Cylindrical Shells*. Pergamon Press, Oxford.

Auld, B. A., 1973. *Acoustic fields and Waves in Solids*. Wiley-Interscience, New York.

Bai, H. 2001,"Elastic Wave Scattering in Cracked Cylinders," *Ph. D. dissertation*, University of Manitoba, Canada.

Bai, H., Shah, A. H., Popplewell, N., and Data, S. K., 2001, "Scattering of Guided Waves by Circumferential Cracks in Steel Pipes," ASME *Journal of Applied Mechanics,* **68**, pp. 619-631.

Bancroft, D., 1941, "The Velocity of Longitudinal Waves in Cylindrical Bars," *The Physical Review*, **59,** p. 588-568.

Bathe, K. J., 1982. *Finite Element Procedures in Engineering Analysis.* Printice-Hall Inc., Englewood Cliffs, New York.

Chandra, R., Kohr, D., Menon, R., Dagum, L., Maydan, D., and McDonald, J., 2001. *Parallel Programming in OpenMP.* Morgan Kaufmann Publishers, San Francisco, CA.

Chang, S. and Mei K. K., 1976, "Application of the Unimoment Method to Electromagnetic Scattering of Dielectric Cylinders," IEEE *Transactions on Antennas and Propagation*, **AP-24**, pp. 35-42

Chree, C., 1889, "The Equation of Isotropic Elastic Solid in Polar and Cylindrical Coordinates, their Solution and Application," *Trans. Cambridge Philosophical Society,* **14**, pp. 250-269.

Datta, S. K., Shah, A. H., and Fortunko, C. M., 1982, "Diffraction of Medium and Long Wavelength Horizontally Polarized Shear Waves by Edge Cracks," *Journal of Applied Physics*, **53**(4), pp. 2895-2903.

Davies, R. M., 1948, "A Critical Study of the Hopkinson Pressure Bar," *Transactions of Royal Philosophical Society of London*, **240**(A), p. 375.

Desai, C. S. and Abel, J. F., 1972. *Introduction to the Finite Element Method: A Numerical Method for Engineering Analysis.* Von Nostrand Reinhold Company, New York.

Fredrick, J. R., 1965. *Ultrasonic Engineering.* John Wiley & Sons, Inc., New York.

Gazis, D. C., 1959, "Three-Dimensional Investigation of the Propagation of Waves in Hollow Circular Cylinders, I. Analytical Foundation, II. Numerical Results," *Journal of the Acoustical Society of America,* **31(5),** pp. 568-578.

Graff, K. F., 1975. *Wave Motion in Elastic Solids.* Calrendon Press, Oxford.

Green, W. A., 1964, "Dispersion Relations for Elastic Waves in Bars," in *Progress in Solid Mechanics* (Eds. Sneddon, I. N. and Hill R.), Vol. 1, Chap. 5, North-Holland Publishing Company, Amsterdam.

Gregory, R. D. and Gladwell, I., 1989, "Axisymmetric Waves in a Semi Infinite Elastic Rod," ASME *Journal of Applied Mechanics*, **42**, pp. 327-337.

Kardestuncer, H. (Ed.), 1987. *Finite Element Handbook.* McGraw-Hill Book Co., New York.

Karunasena, W. M. 1992, "Elastic Waves in Laminated Composite Plates for Application in Ultrasonic Nondestructive Evaluation," *Ph. D. dissertation*, University of Manitoba, Canada.

Karunasena, W. M., Shah, A. H., and Data, S. K., 1991, "Plane-Strain-Wave Scattering by Cracks in Laminated Composite Plates," *Journal of Engineering Mechanics,* **117**(8), pp. 1738-1753.

Kim, Y. Y. and Steele, C. R., 1989, "End Effects and Time-Harmonic Longitudinal Wave Propagation in a Semi-Infinite Solid Cylinder," ASME *Journal of Applied Mechanics*, **56**, pp. 334-346.

Kraut, E. A. 1976, "Review of Theories of Scattering of Elastic Waves by Cracks," IEEE *Transaction on Ultrasonics*, **SU-23**, pp. 162-167.

Lai, J. L., 1971, "Propagation of Harmonic Waves in Composite Elastic Cylinder," *Journal of Acoustical Society of America,* **49**, pp. 220-228.

Lowe, M. J. S., Alleyne, D. N., and Cawley, P., 1998, "The Mode Conversion of a Guided Wave by a Part- Circumferential Notch in Pipe," ASME *Journal of Applied Mechanics*, **65,** pp. 649-656.

McDonald, B. H. and Wexler, A., 1972, "Finite-Element Solution of Unbounded Field Problems," IEEE *Transactions*, **MTT-20** (12), pp. 841-847.

McMaster, R. C., 1959. *Nondestructive Testing Handbook.* Society of Nondestructive Testing, The Ronald Press Company, New York.

McNiven, H. D., 1961, "Extensional Waves in a Semi-Infinite, Elastic Rods," *Journal of the Acoustical Society of America,* **33**, pp. 23-27.

McNiven, H. D., Sackman, J. L., and Shah, A. H., 1963, "Dispersion of Axially Symmetric Waves in Composite, Elastic Rods," *Journal of Acoustical Society of America,* **35**, pp. 1602-1609.

McNiven, H. D. and Shah, A. H., 1967, "The Influence of End Mode on the Resonant Frequencies of Finite, Hollow Elastic Rods," *Journal of Sound and Vibration*, **6,** pp. 8-19.

Mei, K. K., 1974, "Unimoment Method of Solving Antenna and Scattering Problems," IEEE *Transactions on Antennas and Propagation*, **AP-22**, pp. 760-766

Morse, P. M. and Feshback, H., 1953. *Methods of Mathematical Physics: Volume 2.* McGraw-Hill Book Co., New York.

Muller, D. E., 1956, "A Method for Solving Algebraic Equations Using an Automatic Computer," *Mathematical Table and Aids to Computation,* **10**, pp. 208-215.

Oliver, J., 1957, "Elastic Wave Dispersion in a Cylindrical Rod by a Wide-band, Short-duration Pulse Technique," *Journal of Acoustical Society of America,* **29**, pp. 189-194.

Onoe, M., McNiven, H. D., and Mindlin, R. D., 1962, "Dispersion of Axially Symmetric Waves in Elastic Rods," ASME *Journal of Applied Mechanics,* **29,** pp. 729-734.

Pan, E., Rogers, J., Datta, S. K., and Shah, A. H., 1999, "Mode Selection of Guided Waves for Ultrasonic Inspection of Gas Pipelines with Thick Coating," *International Journal of Mechanics of Materials*, **31**, pp. 163-174.

Pochhammer, L., 1876, "Ueber die Fortpflanzungsgeschwindigkeiten Schwingungen in einem Unbegrenzten Isotropen Kreiscylinder," *Zeitschrift für Mathematik*, **81**, pp. 324-336.

Rattanawangcharoen, N., and Shah, A. H., 1992a, "Guided Waves in Laminated Isotropic Circular Cylinders," *Computational Mechanics,* **10,** pp. 97-105.

Rattanawangcharoen, N., and Shah, A. H., 1992b, "Wave Propagation in Laminated Composite Circular Cylinders," *International Journal of Solids and Structures,* **29**(6), pp. 97-105.

Rattanawangcharoen, N., 1993, "Propagation and Scattering of Elastic Waves in Laminated Circular Cylinders," *Ph.D. dissertation*, University of Manitoba, Canada.

Rattanawangcharoen, N., Zhaung, W., Shah, A. H., and Datta, S. K., 1997, "Axisymmetric Guided Waves in Jointed Laminated Cylinders," ASCE *Journal of Engineering Mechanics,* **123**(10), pp. 1020-1026.

Rose, J. L. and Quarry, M. J. 1999, "Feasibility of Ultrasonic Guided Waves for Nondestructive Evaluation of Gas Pipelines," *Gas Research Institute*, Topical Report GRI-99/0076.

Schick, W. and Silverman G., 1995. *Fortran 90 and Engineering Computations*. John Wiley and Sons, New York.

Tan, M. and Auld, B. A. 1980, "Normal Mode Variational Method for the Two- and Three-dimensional Acoustic Scattering in an Isotropic Plate," *1980 Ultrasonic Symposium Procedures,* pp. 587-861.

Zemanek, J., 1972, "An Experimental and Theoretical Investigation of Elastic Wave Propagation in a Cylinder," *Journal of Acoustical Society of America*, **51**(1), pp. 265-283.

Zhaung, W., Shah, A. H. and Datta, S. K. 1997, "Axisymmetric Guided Wave Scattering by Cracks in Welded Steel Pipes," *Journal of Pressure Vessel Technology*, **119**, pp.401-406.

Zienkiewicz, O.C., 1977. *The Finite Element Method.* McGraw-Hill Book Co., London.

Appendix A

Propagator Matrix

Defining:

$$
\begin{aligned}
C_k(1,1) &= \frac{m}{r} Z_m(\alpha r) - \alpha Z_{m+1}(\alpha r), \\
C_k(1,2) &= \xi Z_{m+1}(\beta r), \\
C_k(1,3) &= i\frac{m}{r} Z_m(\beta r), \\
C_k(2,1) &= -i\frac{m}{r} Z_m(\alpha r), \\
C_k(2,2) &= i\xi Z_{m+1}(\beta r), \\
C_k(2,3) &= \beta Z_{m+1}(\beta r) - \frac{m}{r} Z_m(\beta r), \\
C_k(3,1) &= i\xi Z_m(\alpha r), \\
C_k(3,2) &= -i\beta Z_m(\beta r), \\
C_k(3,3) &= 0, \\
C_k(4,1) &= \mu\left\{\left(\frac{2m(m-1)}{r^2} + \left(\xi^2 - \beta^2\right)\right) Z_m(\alpha r) + \frac{2\alpha}{r} Z_{m+1}(\alpha r)\right\},
\end{aligned}
\tag{A.1}
$$

$$C_k(4,2) = 2\mu\xi\left\{\beta Z_m(\beta r) - \frac{(m+1)}{r} Z_{m+1}(\beta r)\right\},$$

$$C_k(4,3) = \frac{2i\mu m}{r}\left\{\frac{(m-1)}{r} Z_m(\beta r) - \beta Z_{m+1}(\beta r)\right\},$$

$$C_k(5,1) = \frac{2i\mu m}{r}\left\{\frac{(m-1)}{r} Z_m(\beta r) - \alpha Z_{m+1}(\beta r)\right\},$$

$$C_k(5,2) = i\mu\xi\left\{\frac{2(m+1)}{r} Z_{m+1}(\beta r) - \beta Z_m(\beta r)\right\},$$

$$C_k(5,3) = \mu\left\{\left(\beta^2 - \frac{2m(m-1)}{r^2}\right) Z_m(\beta r) - \frac{2\beta}{r} Z_{m+1}(\beta r)\right\},$$

$$C_k(6,1) = 2i\mu\xi\left\{\alpha Z_{m+1}(\alpha r) - \frac{m}{r} Z_m(\alpha r)\right\},$$

$$C_k(6,2) = i\mu\left\{\left(\beta^2 - \xi^2\right) Z_{m+1}(\beta r) - \frac{\beta m}{r} Z_m(\beta r)\right\},$$

$$C_k(6,3) = \frac{\mu m\xi}{r} Z_m(\beta r)$$

then the elements of matrix $\boldsymbol{Q}_k$ given in equation (2.29) are:

$$Q_k(i,j) = C_k(i,j) \qquad i = 1,.....,6;\ j = 1,.....,3. \tag{A.2}$$

Here Z_m and Z_{m+1} are $H_m^{(1)}$ and $H_{m+1}^{(1)}$, respectively, and $r = r_k$. The other three columns, i.e. $j = 4,....,6$, can be obtained from the first three columns by replacing the Hankel functions $H_m^{(1)}$ and $H_{m+1}^{(1)}$ by $H_m^{(2)}$ and $H_{m+1}^{(2)}$, respectively.

The element of the three by three matrices $\boldsymbol{R}$ and $\boldsymbol{T}$ in equation (2.40) are:

$$R(i,j) = C_k(i,j), \tag{A.3a}$$

and

$$T(i,j) = C_k(i+3,j), \qquad i = 1,.....3;\ j = 1,.....,3; \tag{A.3b}$$

where Z_m and Z_{m+1} denote J_m and J_{m+1}, respectively, and $r = r_1$.

Appendix B[1]

Sign Convention in the Hybrid Method

B-1. The frequency equation for the cylinder

Consider an isotropic elastic cylinder circular extending from $-\infty$ to $+\infty$ in the z direction. The equations of motion, in an invariant form, are

$$\mu\nabla^2\boldsymbol{U} + (\lambda+\mu)\nabla\nabla\cdot\boldsymbol{U} = \rho\,\partial^2\boldsymbol{U}/\partial t^2\,, \tag{B.1}$$

where $\boldsymbol{U}$ is the displacement vector, ρ is the mass density, λ and μ are Lame's constants and ∇^2 is the three-dimensional Laplace operator. The eigenvalue problem consists of finding solutions $\boldsymbol{U}$ that satisfy equation (B.1) and the boundary conditions:

$$\sigma^{rr} = 0, \quad \sigma^{r\theta} = 0, \quad \sigma^{rz} = 0. \tag{B.2}$$

The formulation of the displacements and stresses in terms of the potential functions Φ and $\boldsymbol{H}$ is:

---

[1] Appendix B is courtesy of Dr. Hao Bai, a research associate in the Civil and Geological Engineering Department, University of Manitoba.

$$\boldsymbol{U} = \nabla\Phi + \nabla\times\boldsymbol{H}, \quad \nabla\cdot\boldsymbol{H} = F(\boldsymbol{x},t) \tag{B.3}$$

where $F(\boldsymbol{x},t)$ is an arbitrary function. The potentials $\boldsymbol{\Phi}$ and $\boldsymbol{H}$ satisfy the scalar and vector wave equations,

$$\nabla^2\Phi = \frac{1}{c_p^2}\frac{\partial^2\Phi}{\partial t^2}, \quad \nabla^2\boldsymbol{H} = \frac{1}{c_s^2}\frac{\partial^2\boldsymbol{H}}{\partial t^2}, \tag{B.4}$$

where c_p and c_s are the dilatational and distortional wave speeds, respectively. They are given by

$$c_p^2 = \frac{\lambda+2\mu}{\rho} \quad \text{and} \quad c_s^2 = \frac{\mu}{\rho}.$$

In expanded form, $\nabla^2\Phi$ and $\nabla^2\boldsymbol{H}$ are

$$\nabla^2\Phi = \frac{\partial^2\Phi}{\partial r^2} + \frac{1}{r}\frac{\partial\Phi}{\partial r} + \frac{1}{r^2}\frac{\partial^2\Phi}{\partial\theta^2} + \frac{\partial^2\Phi}{\partial z^2}$$

$$\nabla^2\boldsymbol{H} = \left(\nabla^2 H_r - \frac{H_r}{r^2} - \frac{2}{r^2}\frac{\partial H_\theta}{\partial\theta}\right)\boldsymbol{e}_r + \left(\nabla^2 H_\theta - \frac{H_\theta}{r^2} + \frac{2}{r^2}\frac{\partial H_r}{\partial\theta}\right)\boldsymbol{e}_\theta + \nabla^2 H_z\boldsymbol{e}_z.$$

Assume that solutions of the wave equations (B.4) take the form:

$$\Phi = f_\Phi(r)e^{jpm\theta}e^{j(q\xi z+\omega t)} \tag{B.5a}$$

$$H_r = f_r(r)e^{jpm\theta}e^{j(q\xi z+\omega t)} \tag{B.5b}$$

$$H_\theta = f_\theta(r)e^{jpm\theta}e^{j(q\xi z+\omega t)} \tag{B.5c}$$

$$H_z = f_z(r)e^{jpm\theta}e^{j(q\xi z+\omega t)} \tag{B.5d}$$

where $p,\ q = \pm 1,\ m \geq 0$. The $e^{jpm\theta}e^{j(q\xi z+\omega t)}$ is suppressed in the sequel. Then

$$f_\Phi'' + \frac{1}{r} f_\Phi' + (\alpha^2 - \frac{m^2}{r^2}) f_\Phi = 0 \qquad \text{(B.6a)}$$

$$f_z'' + \frac{1}{r} f_z' + (\beta^2 - \frac{m^2}{r^2}) f_z = 0 \qquad \text{(B.6b)}$$

$$f_r'' + \frac{1}{r} f_r' + \beta^2 f_r - \frac{1}{r^2}(m^2 f_r + 2jpmf_\theta + f_r) = 0 \qquad \text{(B.6c)}$$

$$f_\theta + \frac{1}{r} f_\theta' + \beta^2 f_\theta - \frac{1}{r^2}(m^2 f_\theta - 2jpmf_r + f_\theta) = 0 \qquad \text{(B.6d)}$$

where a prime superscript denotes differentiation with respect to r and

$$\alpha^2 = \omega^2/c_p^2 - \xi^2, \quad \beta^2 = \omega^2/c_s^2 - \xi^2.$$

By considering the property of gauge invariance, it may be assumed that

$$f_\theta = -jpf_r, \quad f_r = jpf_\theta.$$

Consequently, from equation (B.6c), f_r satisfies:

$$f_r'' + \frac{1}{r} f_r' + \left[\beta^2 - \frac{(m+1)^2}{r^2} \right] f_r = 0. \qquad \text{(B.7)}$$

The scalar components of $\boldsymbol{U}$ are given by:

$$\begin{aligned} u^r &= \frac{\partial \Phi}{\partial r} + \frac{1}{r}\frac{\partial H_z}{\partial \theta} - \frac{\partial H_\theta}{\partial z} \\ u^\theta &= \frac{1}{r}\frac{\partial \Phi}{\partial \theta} + \frac{\partial H_r}{\partial z} - \frac{\partial H_z}{\partial r} \\ u^z &= \frac{\partial \Phi}{\partial z} - \frac{1}{r}\frac{\partial H_r}{\partial \theta} + \frac{H_\theta}{r} + \frac{\partial H_\theta}{\partial r}. \end{aligned} \qquad \text{(B.8)}$$

The displacement components on the other hand, are derived by substituting equation (B.5) into equation (B.8), so that:

$$\begin{aligned} u^r &= f'_\Phi - pq\xi f_r + \tfrac{jpm}{r} f_z \\ u^\theta &= \tfrac{jpm}{r} f + jq\xi f_r - f'_z \\ u^z &= jq\xi f_\Phi - jp\left(f'_r + \tfrac{m+1}{r} f_r\right). \end{aligned} \tag{B.9}$$

The strain components are given generally by,

$$\varepsilon^{rr} = \frac{\partial u^r}{\partial r}, \quad \varepsilon^{\theta\theta} = \frac{u^r}{r} + \frac{1}{r}\frac{\partial u^\theta}{\partial \theta}, \quad \varepsilon^{zz} = \frac{\partial u^z}{\partial z}$$

$$2\varepsilon^{r\theta} = \frac{1}{r}\frac{\partial u^r}{\partial \theta} + \frac{\partial u^\theta}{\partial r} - \frac{u^\theta}{r}, \quad 2\varepsilon^{rz} = \frac{\partial u^r}{\partial z} + \frac{\partial u^z}{\partial r}, \quad 2\varepsilon^{\theta z} = \frac{\partial u^\theta}{\partial z} + \frac{1}{r}\frac{\partial u^z}{\partial \theta}$$

so that

$$\begin{aligned} \varepsilon^{rr} &= f''_\Phi - pq\xi f'_r + \tfrac{jpm}{r}\left(f'_z - \tfrac{1}{r} f_z\right) \\ \varepsilon^{\theta\theta} &= \left(\tfrac{1}{r} f'_\Phi - \tfrac{m^2}{r^2} f_\Phi\right) - pq\xi \tfrac{m+1}{r} f_r - \tfrac{jpm}{r}\left(f'_z - \tfrac{1}{r} f_z\right) \\ \varepsilon^{zz} &= -\xi^2 f_\Phi + pq\xi\left(f'_r + \tfrac{m+1}{r} f_r\right) \\ \varepsilon^{r\theta} &= \tfrac{jpm}{r}\left(f'_\Phi - \tfrac{1}{r} f_\Phi\right) + \frac{j\xi}{2}\left(f'_r - \tfrac{m+1}{r} f_r\right) + \frac{1}{2}\left(-f''_z + \tfrac{1}{r} f'_z - \tfrac{m2}{r^2} f_z\right) \\ \varepsilon^{rz} &= jq\xi f'_\Phi - \tfrac{jp}{2r}\left(f''_r + \tfrac{m+1}{r} f'_r + (\xi^2 - \tfrac{m+1}{r^2}) f_r\right) - pq\xi \tfrac{m}{2r} f_z \\ \varepsilon^{\theta z} &= -pq\xi \tfrac{m}{r} f_\Phi + \frac{1}{2}\left(\tfrac{m}{r} f'_r - (\xi^2 - \tfrac{m+1}{r^2}) f_r\right) - \frac{1}{2} jq\xi f'_z. \end{aligned} \tag{B.10}$$

Hence the dilatation is given by

$$\Delta = \varepsilon^{rr} + \varepsilon^{\theta\theta} + \varepsilon^{zz} = -\left(\alpha^2 + \xi^2\right) f_\Phi.$$

The stresses are derived from Hooke's law, $\sigma^{ij} = \lambda\Delta\delta_{ij} + 2\mu\varepsilon^{ij}$, as:

$$
\begin{aligned}
\sigma^{rr} &= \mu\left[-\tfrac{2}{r} f_\Phi' + \left(\xi^2 - \beta^2 + \tfrac{2m^2}{r^2}\right) f_\Phi - 2pq\xi f_r' + 2\tfrac{jpm}{r}\left(f_z' - \tfrac{1}{r} f_z\right)\right] \\
\sigma^{\theta\theta} &= \mu\left[\tfrac{2}{r} f_\Phi' + \left(2\alpha^2 - \beta^2 + \xi^2 - \tfrac{2m^2}{r^2}\right) f_\Phi - 2pq\xi \tfrac{m+1}{r} f_r - 2\tfrac{jpm}{r}\left(f_z' - \tfrac{1}{r} f_z\right)\right] \\
\sigma^{zz} &= \mu\left[\left(2\alpha^2 - \beta^2 - \xi^2\right) f_\Phi + 2pq\xi\left(f_r' + \tfrac{m+1}{r} f_r\right)\right] \\
\sigma^{r\theta} &= \mu\left[2\tfrac{jpm}{r}\left(f_\Phi' - \tfrac{1}{r} f_\Phi\right) + jq\xi\left(f_r' - \tfrac{m+1}{r} f_r\right) + \left(\tfrac{2}{r} f_z' + (\beta^2 - \tfrac{2m^2}{r^2}) f_z\right)\right] \\
\sigma^{rz} &= \mu\left[2jq\xi f_\Phi' - jp\left(\tfrac{m}{r} f_r' + (\xi^2 - \beta^2 + \tfrac{m^2+m}{r^2}) f_r\right) - pq\xi \tfrac{m}{r} f_z\right] \\
\sigma^{\theta z} &= \mu\left[-2pq\xi \tfrac{m}{r} f_\Phi + \left(\tfrac{m}{r} f_r' + (\tfrac{m^2+m}{r^2} - \xi^2) f_r\right) - jq\xi f_z'\right].
\end{aligned}
\tag{B.11}
$$

For a solid rod,

$$
\begin{aligned}
f_\Phi(r) &= C_1 J_m(\alpha r) \\
f_r(r) &= qC_2 J_{m+1}(\beta r) \\
f_z(r) &= C_3 J_m(\beta r)
\end{aligned}
\tag{B.12}
$$

where $C_i, i = 1,2,3$ are arbitrary constants. The frequency equation is derived from the boundary condition (B.2), which can be rewritten as:

$$
\begin{aligned}
\sigma^{rr} &= P_{11}C_1 + P_{12}C_2 + P_{13}C_3 = 0 \\
\sigma^{r\theta} &= P_{21}C_1 + P_{22}C_2 + P_{23}C_3 = 0, \\
\sigma^{rz} &= q\left(P_{31}C_1 + P_{32}C_2 + P_{33}C_3\right) = 0.
\end{aligned}
\tag{B.13}
$$

It can be seen from the equation (B.13) that the coefficients $C_i, i = 1,2,3$ do not change their signs with a change in the sign of q. Furthermore,

$$
\begin{aligned}
u^r(r,\theta,z,t;q) &= u^r(r,\theta,z,t) \\
u^\theta(r,\theta,z,t;q) &= u^\theta(r,\theta,z,t) \\
u^z(r,\theta,z,t;q) &= u^z(r,\theta,z,t)\, q
\end{aligned}
\tag{B.14}
$$

$$\begin{aligned}\sigma^{zr}(r,\theta,z,t;q)&=\sigma^{zr}(r,\theta,z,t)q\\ \sigma^{z\theta}(r,\theta,z,t;q)&=\sigma^{z\theta}(r,\theta,z,t)q\\ \sigma^{zz}(r,\theta,z,t;q)&=\sigma^{zz}(r,\theta,z,t).\end{aligned}\tag{B.15}$$

Variables without a subscript q as well as the matrices P, D and T are given in section B-2 of this Appendix. The tractions at the cross section, $z=const$ which has a normal vector $\boldsymbol{n}=-\boldsymbol{e}_z$, are given by:

$$\begin{aligned}p^{r}(r,\theta,z,t;q)&=-\sigma^{zr}(r,\theta,z,t)q\\ p^{\theta}(r,\theta,z,t;q)&=-\sigma^{z\theta}(r,\theta,z,t)q\\ p^{z}(r,\theta,z,t;q)&=-\sigma^{zz}(r,\theta,z,t).\end{aligned}\tag{B.16}$$

As $q=-1$ for the reflected wave field and $q=1$ for the incident and transmitted wave fields, then:

$$u^{r,I}=u^{r,-}=u^{r,+},\quad u^{\theta,I}=u^{\theta,-}=u^{\theta,+},\quad u^{z,I}=u^{z,-}=-u^{z,+},\tag{B.17}$$

$$p^{r,I}=p^{r,-}=-p^{r,+},\quad p^{\theta,I}=p^{\theta,-}=-p^{\theta,+},\quad p^{z,I}=p^{z,-}=p^{z,+}.\tag{B.18}$$

The corresponding relations in the plane of the normal vector, $\boldsymbol{n}=\boldsymbol{e}_z$, are:

$$u^{r,I}=u^{r,-}=u^{r,+},\quad u^{\theta,I}=u^{\theta,-}=u^{\theta,+},\quad u^{z,I}=u^{z,-}=-u^{z,+},\tag{B.19}$$

$$p^{r,I}=p^{r,-}=p^{r,+},\quad p^{\theta,I}=p^{\theta,-}=p^{\theta,+},\quad p^{z,I}=p^{z,-}=-p^{z,+}.\tag{B.20}$$

B-2 Supplement

The displacement and stress components appearing in equations (B.14) and (B.15) are:

$$
\begin{aligned}
u^r &= D_{11}C_1 + D_{12}C_2 + D_{13}C_3 \\
u^\theta &= D_{21}C_1 + D_{22}C_2 + D_{23}C_3, \\
u^z &= D_{31}C_1 + D_{32}C_2
\end{aligned}
\tag{B-21}
$$

$$
\begin{aligned}
\sigma^{rz} &= \mu\left[T_{11}C_1 + T_{12}C_2 + T_{13}C_3\right] \\
\sigma^{\theta z} &= \mu\left[T_{21}C_1 + T_{22}C_2 + T_{23}C_3\right] \\
\sigma^{zz} &= \mu\left[T_{31}C_1 + T_{32}C_2 + T_{33}C_3\right]
\end{aligned}
\tag{B-22}
$$

in terms of $C_i \ (i = 1..3)$ where $D_{ij} \ (i, j = 1..3)$ are defined as:

$$
\begin{aligned}
D_{11} &= \tfrac{m}{r} J_m(\alpha r) - \alpha J_{m+1}(\alpha r), \\
D_{12} &= -p\xi J_{m+1}(\beta r), \\
D_{13} &= \tfrac{jpm}{r} J_m(\beta r), \\
D_{21} &= \tfrac{jpm}{r} J_m(\alpha r), \\
D_{22} &= j\xi J_{m+1}(\beta r), \\
D_{23} &= -\tfrac{m}{r} J_m(\beta r) + \beta J_{m+1}(\beta r), \\
D_{31} &= j\xi J_m(\alpha r), \\
D_{32} &= -jp\beta J_m(\beta r), \\
D_{33} &= 0.
\end{aligned}
\tag{B.23}
$$

Furthermore, the $T_{ij} \ (i, j = 1..3)$ are:

$$
\begin{aligned}
T_{11} &= -2i\xi\left(\alpha J_{m+1}(\alpha r) - \tfrac{m}{r} J_m(\alpha r)\right), \\
T_{12} &= -ip\left(\tfrac{\beta m}{r} J_m(\beta r) + \left(\xi^2 - \beta^2\right) J_{m+1}(\beta r)\right), \\
T_{13} &= -\tfrac{pm\xi}{r} J_m(\beta r), \\
T_{21} &= -2\tfrac{pm\xi}{r} J_m(\alpha r), \\
T_{22} &= \tfrac{\beta m}{r} J_m(\beta r) - \xi^2 J_{m+1}(\beta r), \\
T_{23} &= -i\xi\left(\beta J_{m+1}(\beta r) - \tfrac{m}{r} J_m(\beta r)\right), \\
T_{31} &= \left(2\alpha^2 - \beta^2 - \xi^2\right) J_m(\alpha r), \\
T_{32} &= 2p\xi\beta J_m(\beta r), \\
T_{33} &= 0.
\end{aligned}
\tag{B-24}
$$

The elements of the matrix P appearing in equation (B.13) are:

$$
\begin{aligned}
P_{11} &= \left(\xi^2 - \beta^2 + 2\tfrac{m^2-m}{r^2}\right) J_m(\alpha r) + \tfrac{2}{r} J_{m+1}(\alpha r), \\
P_{12} &= -2p\xi\left(\beta J_m(\beta r) - \tfrac{m+1}{r} J_{m+1}(\beta r)\right), \\
P_{13} &= -2\tfrac{jpm}{r}\left(\beta J_{m+1}(\beta r) - \tfrac{m-1}{r} J_m(\beta r)\right) \\
P_{21} &= -2\tfrac{jpm}{r}\left(\alpha J_{m+1}(\alpha r) - \tfrac{m-1}{r} J_m(\alpha r)\right), \\
P_{22} &= j\xi\left(\beta J_m(\beta r) - 2\tfrac{m+1}{r} J_{m+1}(\beta r)\right), \\
P_{23} &= \left(\beta^2 - 2\tfrac{m^2-m}{r^2}\right) J_m(\beta r) - \tfrac{2\beta}{r} J_{m+1}(\beta r), \\
P_{31} &= -2j\xi\left(\alpha J_{m+1}(\alpha r) - \tfrac{m}{r} J_m(\alpha r)\right), \\
P_{32} &= -jp\left(\tfrac{\beta m}{r} J_m(\beta r) + \left(\xi^2 - \beta^2\right) J_{m+1}(\beta r)\right), \\
P_{33} &= -\tfrac{pm\xi}{r} J_m(\beta r).
\end{aligned}
\tag{B.25}
$$

Appendix C

Shape Functions and Derivatives for the 20-node Brick Element

The shape functions of the twenty-node brick element, see Figure C.1, are (Kardestuncer 1987):

$$n_i = (1/8)(1-\xi_i\xi)(1+\eta_i\eta)(1+\zeta_i\zeta)(\xi_i\xi+\eta_i\eta+\zeta_i\zeta-2) \quad \text{(C.1a)}$$

$$i = 1,3,5,7,13,15,17,19$$

$$n_i = (1/4)(1-\xi^2)(1+\eta_i\eta)(1+\zeta_i\zeta) \quad \text{(C.1b)}$$

$$i = 2,6,14,18$$

$$n_i = (1/4)(1-\eta^2)(1+\xi_i\xi)(1+\zeta_i\zeta) \quad \text{(C.1c)}$$

$$i = 4,8,16,20$$

$$n_i = (1/4)(1-\zeta^2)(1+\xi_i\xi)(1+\eta_i\eta) \quad \text{(C.1d)}$$

$$i = 9,10,11,12$$

Their derivatives n_i^{ξ}, n_i^{η} and n_i^{ζ} (with respect to ξ, η, and ζ respectively) are:

$$n_i^{\xi} = (1/8)(1+\eta_i\eta)(1+\zeta_i\zeta)\{\xi_i(\xi_i\xi+\eta_i\eta+\zeta_i\zeta-2)\} \quad \text{(C.2a)}$$

$$i = 1,3,5,7,13,15,17,19$$

$$n_i^{\xi} = (1/4)(1+\eta_i\eta)(1+\zeta_i\zeta)(1-2\xi) \quad \text{(C.2b)}$$

$$i = 2,6,14,18$$

$$n_i^{\xi} = (1/4)(1-\eta^2)(1+\zeta_i\zeta)\xi_i \quad \text{(C.2c)}$$

$$i = 4,8,16,20$$

$$n_i^{\xi} = (1/4)(1-\zeta^2)(1+\eta_i\eta)\xi_i \quad \text{(C.2d)}$$

$$i = 9,10,11,12$$

whereas

$$n_i^{\eta} = (1/8)(1+\xi_i\xi)(1+\zeta_i\zeta)\{\eta_i(\xi_i\xi+\eta_i\eta+\zeta_i\zeta-2)+\eta_i(1+\eta_i\eta)\} \quad \text{(C.3a)}$$

$$i = 1,3,5,7,13,15,17,19$$

$$n_i^{\eta} = (1/4)(1+\xi_i\xi)(1+\zeta_i\zeta)\eta_i \quad \text{(C.3b)}$$

$$i = 2,6,14,18$$

$$n_i^{\eta} = (1/4)(1-\xi_i\xi)(1+\zeta_i\zeta)(1-2\eta) \quad \text{(C.3c)}$$

$$i = 4,8,16,20$$

$$n_i^{\eta} = (1/4)(1-\zeta^2)(1+\xi_i\xi)\eta_i \quad \text{(C.3d)}$$

$$i = 9,10,11,12$$

and

$$n_i^{\zeta} = (1/8)(1+\xi_i\xi)(1+\eta_i\eta)\{\zeta_i(\xi_i\xi+\eta_i\eta+\zeta_i\zeta-2)+\zeta_i(1+\zeta_i\zeta)\} \quad \text{(C.4a)}$$

$$i = 1,3,5,7,13,15,17,19$$

$$n_i^{\zeta} = (1/4)(1+\xi_i\xi)(1+\eta_i\eta)\zeta_i \quad \text{(C.4b)}$$

$$i = 2,6,14,18$$

$$n_i^{\zeta} = (1/4)(1-\eta^2)(1+\xi_i\xi)\zeta_i \quad \text{(C.4c)}$$

$$i = 4,8,16,20$$

$$n_i^{\zeta} = (1/4)(1+\xi_i\xi)\eta_i(1-2\zeta) \quad \text{(C.4d)}$$

$$i = 9,10,11,12\,.$$

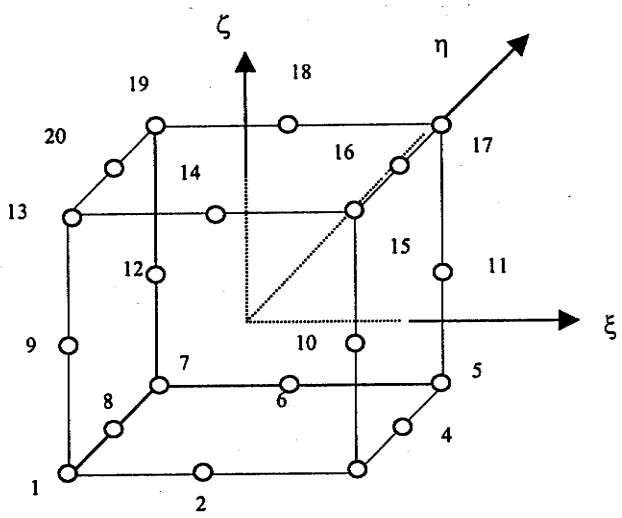

Figure C.1. 20-node brick element

Appendix D

Condensation Formulae

The matrix coefficients $S_{ij}^{*}\ (i=1..4, j=1..4, B)$ in equations (4.2) and (4.3) are given by:

$$S_{11}^{*} = S_{11} \tag{D. 1}$$

$$S_{12}^{*} = S_{12} \tag{D. 2}$$

$$S_{13}^{*} = S_{13} \tag{D. 3}$$

$$S_{22}^{*} = S_{22} - S_{12}^{*\,T} S_{11}^{*\,-1} S_{12}^{*} \tag{D. 4}$$

$$S_{23}^{*} = S_{23} - S_{12}^{*\,T} S_{11}^{*\,-1} S_{13}^{*} \tag{D. 5}$$

$$S_{33}^{*} = S_{33} - S_{13}^{*\,T} S_{11}^{*\,-1} S_{13}^{*} - S_{23}^{*\,T} S_{22}^{*\,-1} S_{23}^{*} \tag{D. 6}$$

$$S_{34}^{*} = S_{34} \tag{D. 7}$$

$$S_{3B}^{*} = S_{3B} \tag{D. 8}$$

$$S_{44}^{*} = S_{44} - S_{34}^{*\,T} S_{33}^{*\,-1} S_{34}^{*} \tag{D. 9}$$

and

$$S_{4B}^{*} = S_{4B} - S_{34}^{*\,T} S_{33}^{*\,-1} S_{3B}^{*} \ . \tag{D.10}$$